Monthly Notices
of the
ROYAL ASTRONOMICAL SOCIETY

MNRAS **490,** 3806–3823 (2019)
Advance Access publication 2019 October 23

doi:10.1093/mnras/stz2878

A PSF-based Approach to TESS High quality data Of Stellar clusters (PATHOS) – I. Search for exoplanets and variable stars in the field of 47 Tuc

D. Nardiello [1,2]★ L. Borsato [1,2] G. Piotto,[1,2] L. S. Colombo [1] E. E. Manthopoulou,[1] L. R. Bedin [2] V. Granata,[1] G. Lacedelli,[1] M. Libralato [3] L. Malavolta [4] M. Montalto[1,2] and V. Nascimbeni [1,2]

[1]*Dipartimento di Fisica e Astronomia 'Galileo Galilei', Università di Padova, Vicolo dell'Osservatorio 3, I-35122, Padova, Italy*
[2]*Istituto Nazionale di Astrofisica - Osservatorio Astronomico di Padova, Vicolo dell'Osservatorio 5, I-35122, Padova, Italy*
[3]*Space Telescope Science Institute, 3800 San Martin Drive, Baltimore, MD 21218, USA*
[4]*Istituto Nazionale di Astrofisica - Osservatorio Astronomico di Catania, Via S. Sofia 78, I-95123, Catania, Italy*

Accepted 2019 October 4. Received 2019 September 19; in original form 2019 June 12

ABSTRACT

The *TESS* mission will survey ∼85 per cent of the sky, giving us the opportunity of extracting high-precision light curves of millions of stars, including stellar cluster members. In this work, we present our project 'A PSF-based Approach to TESS High quality data Of Stellar clusters' (PATHOS), aimed at searching and characterize candidate exoplanets and variable stars in stellar clusters using our innovative method for the extraction of high-precision light curves of stars located in crowded environments. Our technique of light-curve extraction involves the use of empirical point spread functions (PSFs), an input catalogue and neighbour-subtraction. The PSF-based approach allows us to minimize the dilution effects in crowded environments and to extract high-precision photometry for stars in the faint regime ($G > 13$). For this pilot project, we extracted, corrected, and analysed the light curves of 16 641 stars located in a dense region centred on the globular cluster 47 Tuc. We were able to reach the *TESS* magnitude $T \sim 16.5$ with a photometric precision of ∼1 per cent on the 6.5-h time-scale; in the bright regime we were able to detect transits with depth of ∼34 parts per million. We searched for variables and candidate transiting exoplanets. Our pipeline detected one planetary candidate orbiting a main-sequence star in the Galactic field. We analysed the period–luminosity distribution for red-giant stars of 47 Tuc and the eclipsing binaries in the field. Light curves are uploaded on the Mikulski Archive for Space Telescopes under the project PATHOS.

Key words: techniques: image processing – techniques: photometric – stars: variables: general – globular clusters: individual: NGC 104.

1 INTRODUCTION

In the last two decades, more than 4000 exoplanets[1] have been discovered and confirmed using spectroscopic and photometric studies. More than 75 per cent exoplanets have been found using the transit method; a strong contribution to this research area came from pioneering photometric surveys, carried out both with ground based (e.g. SuperWASP; Pollacco et al. 2006) and space telescopes (e.g. *CoRoT*; Baglin et al. 2006). In last years, the *Kepler* main mission (Borucki et al. 2010) and the reinvented *Kepler/K2* mission (Howell et al. 2014), allowed the astronomical community to develop new techniques to extract and analyse high precision light curves of stars in many Galactic fields and to find thousands of new exoplanets and variable stars (see e.g. Vanderburg & Johnson 2014; Armstrong et al. 2016; Aigrain, Parviainen & Pope 2016; Barros, Demangeon & Deleuil 2016; Libralato et al. 2016a).

Nevertheless, to date only a few confirmed planets have been found to orbit stars in stellar clusters (e.g. Quinn et al. 2012, 2014; Brucalassi et al. 2014, 2017; Malavolta et al. 2016; Mann et al. 2018). Stellar clusters give us an unique opportunity to understand how exoplanets have formed and evolved. Properties of stars in stellar clusters (e.g. mass, radius, age, and chemical composition) can generally be more reliably measured than for many field stars. For this reason, the discovery and characterization of exoplanets

★ E-mail: domenico.nardiello@unipd.it
[1]http://exoplanets.eu/

orbiting stars in stellar clusters allow us to correlate planet and hosting star properties. Moreover, because stellar clusters' ages span over a wide range that goes from few Myrs up to ten Gyrs, the analysis of exoplanets in different stellar clusters allows us to understand how exoplanets have formed and evolved. In addition, the different chemical properties of the stellar clusters give us the opportunity to understand how the environment has affected the exoplanets' life.

Despite all these advantages, a few exoplanets have been found in stellar clusters because only few clusters have been studied with *Kepler* and/or spectroscopic surveys; indeed, searches for exoplanets orbiting stellar cluster members have been hampered by observational difficulties because of the crowding. For this reason, appropriate techniques for the extraction of high-precision light curves of stars in dense environments are mandatory. Recently, studies based on the extraction of light curves from *Kepler* data of open clusters using the point spread function (PSF) approach (Libralato et al. 2016a) or the differential image analysis (Soares-Furtado et al. 2017) have allowed us to obtain high precision photometric time series for very faint stars located in crowded environments.

In the last year, *Kepler* passed the baton to the *Transiting Exoplanet Survey Satellite* (*TESS*; Ricker et al. 2015), a NASA all-sky survey mission aimed at searching exoplanets around bright stars. During its 2-yr mission, *TESS* will observe about 85 per cent of the sky in 27-d sectors, each one covering 24 × 96 deg^2 and most of them containing hundreds of stellar clusters. In every sector, about 20 000 stars are observed in short-cadence mode (2 min). In addition, *TESS* produces onboard stacked images of the entire field of view, with a cadence of 30 min (full-frame images; FFIs). The FFIs allow us to extract light curves for all objects with $V \lesssim 17$ that fall within the field of view of each sector, giving us not only the possibility to widen the search of exoplanets to a huge number of stars, but also to produce results in other fields, like asteroseismology, analysis of Solar System objects (Pál, Molnár & Kiss 2018), variable stars, supernovae (e.g. Vallely et al. 2019), and other Galactic and extragalactic sources.

In this work, we present our project 'A PSF-based Approach to TESS High quality data Of Stellar clusters' (PATHOS), aimed at extracting high precision light curves of sources in stellar clusters in order to find candidate exoplanets and variable stars. For this project, we apply our expertise on PSF photometry and astrometry on images of crowded fields. In fact, because of the sampling of *TESS* (∼21 arcsec/pixel), also sparse stellar clusters appear to be crowded on *TESS* images. In our previous works (e.g. Nardiello et al. 2015; Libralato et al. 2016a), we demonstrated that by using as input a high-resolution astrophotometric catalogue and empirical PSFs, we are able to measure the flux of each target star in the catalogue with extreme accuracy, after subtracting all its neighbour stars. Using the PSF-based approach we are able to: (1) extract the light curves of stars in crowded regions; (2) minimize the light-contamination effects due to neighbour stars, improving the photometric precision; (3) extract light curves of faint stars, increasing the number of analysable objects.

In this work, we apply for the first time the PSF-based approach to *TESS* data, in order to extract high-precision light curves of sources in a very crowded field centred on the globular cluster NGC 104 (47 Tuc). In Section 2, we describe our pipeline for the extraction of raw light curves and their correction. The description of the finding, vetting, and modelling of candidate exoplanets is reported in Section 3. Section 4 is a description of the procedure used to find and analyse variable stars. In Section 5, we compare our pipeline with the most advanced, publicly available pipeline for the extraction of light curves from FFIs. The public data release discussion and a summary of this work are reported in Sections 6 and 7, respectively.

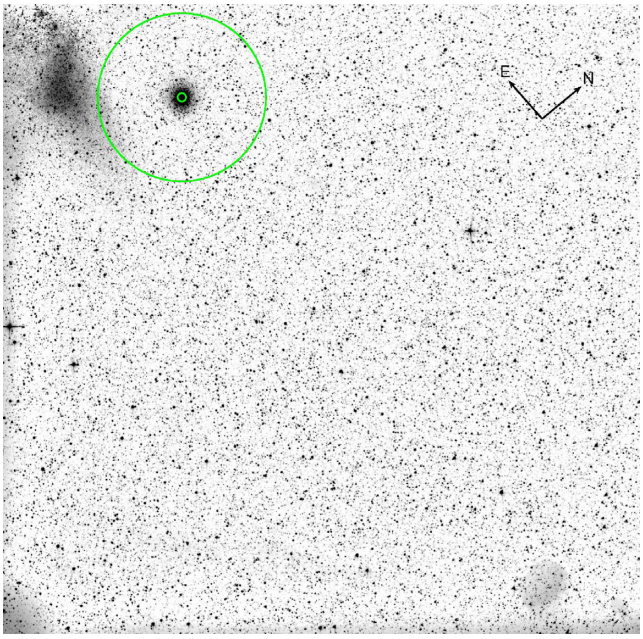

Figure 1. Field of view covered by CCD 2 of Camera 3 in Sector-1. The figure shows the stacked image obtained by combining 1282 *TESS* exposures. The green annulus are the inner and outer bounds of the region containing the stars for which we extracted the light curves ($0.075 \leq R \leq 1.5$ degree).

2 FROM FULL FRAME IMAGES TO LIGHT CURVES

For this pilot work, we used FFIs collected in Sector-1. FFIs are obtained on board by co-adding series of 2 s exposures into a 30 min exposure time image. Observations have been carried out by *TESS* between 2018 July 25 and 2018 August 22 and cover ∼27.83 d, during which 1282 usable FFIs were generated. The target of this work, 47 Tuc, is located on the CCD 2 of Camera 3. As described in the next Sections, we have extracted the light curves for the stars located in an annulus with $0.075 \leq R \leq 1.5$ deg from 47 Tuc centre (as shown in Fig. 1).

2.1 Empirical point spread functions

For our work, it is mandatory to compute the best PSF models for each image, both for the extraction of high precision photometry and for the subtraction of the neighbour stars, as explained in Section 2.3.

The PSFs of the *TESS* cameras are highly variable among the large field of view of each CCD (12 × 12 deg^2). To model the PSFs, we used the empirical approach developed by Anderson et al. (2006), adapting the code used for the data collected with the ESO/MPI wide-field Imager to *TESS* images. To take into account the spatial variation of the PSF, we divided each image

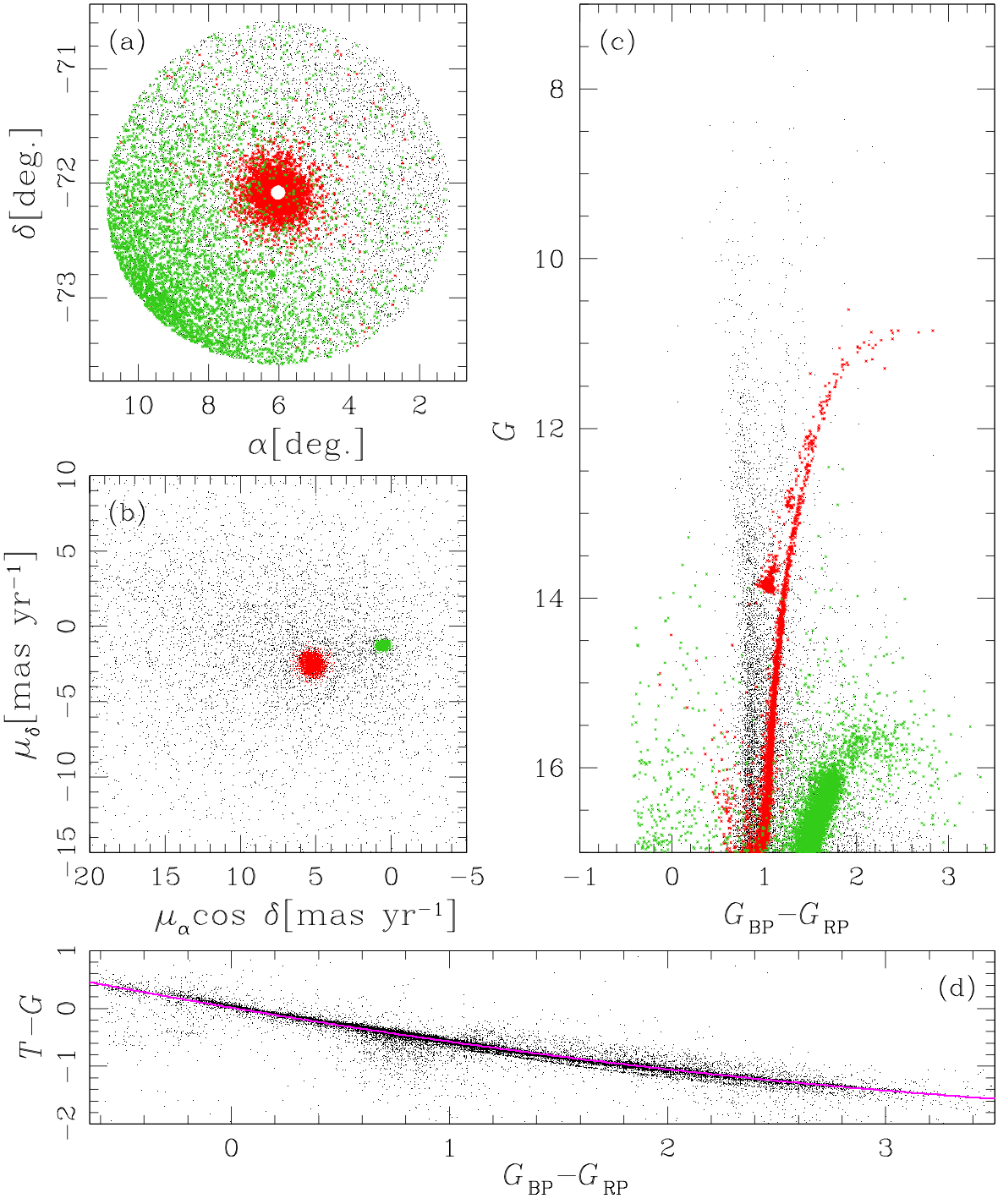

Figure 2. Overview of the Gaia DR2 input catalogue used in this work: panel (a) plots the (α, δ)-coordinates of the sources in the catalogue; panel (b) shows the absolute proper motion distribution for all the stars in the catalogue; panel (c) gives the G versus $G_{\rm BP} - G_{\rm RP}$ CMD for the stars in the catalogue; panel (d) shows the $T - G$ versus $G_{\rm BP} - G_{\rm RP}$ distribution for the stars observed by *TESS* in the first seven sectors. In magenta, the relation adopted to transform *TESS* magnitudes in *Gaia* magnitudes. Red and green points in panels (a)–(c) are stars with high probability to be 47 Tuc and SMC members, respectively.

in a grid of 9 × 9 regions. We empirically computed the PSF models independently in each region using bright, not saturated, isolated stars. Each PSF model is defined on a grid of 201 × 201 points and is super-sampled by a factor 4 with respect to the image pixel.

Adopting this approach, for each position of the CCD we can extract the best, local PSF model by using a bilinear interpolation of the four closest PSFs.

2.2 The input catalogue

For the extraction of the light curves, we need an input catalogue that contains the positions and the magnitudes of the stars in the analysed field. We adopted as input catalogue the Gaia DR2 catalogue (Gaia Collaboration et al. 2018). We excluded from the catalogue all the sources with $G > 17$ because they are too faint to be measured by *TESS* (the total flux is $<30\ e^-\ {\rm s}^{-1}$). For this work, we

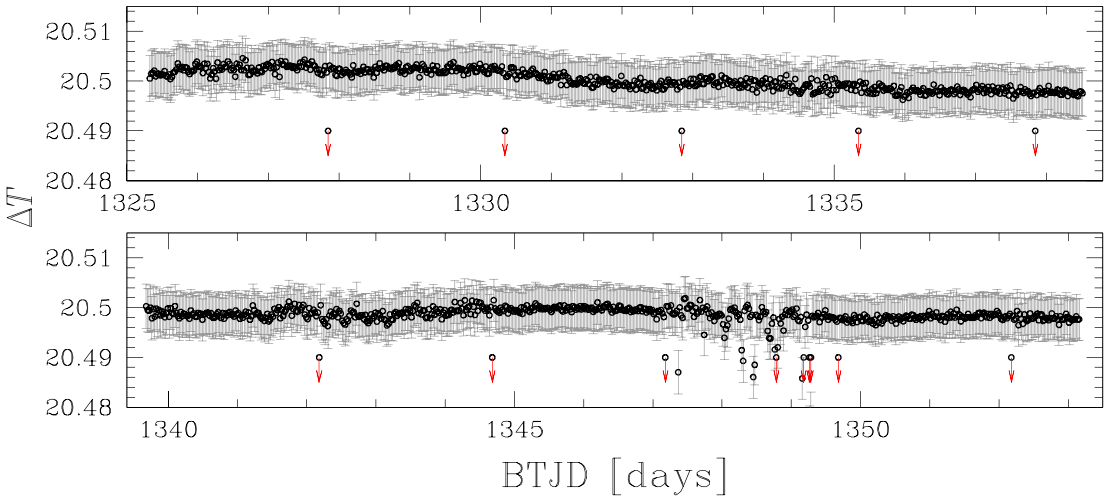

Figure 3. Variation of the zero-point between *TESS* calibrated and instrumental magnitude for Sector-1 *TESS* observations. Red arrows indicate the points that are out of the plot limits.

considered the stars located in a circular region centred in $(\alpha_0, \delta_0) = (6.022\,329, -72.081\,444)$, i.e. on the centre of 47 Tuc (Goldsbury et al. 2010), and with radius $R = 1.5$ deg ($\sim 2 \times$ the tidal radius of 47 Tuc). We excluded from the input catalogue all the stars with $R \leq 0.075$ deg because the TESS images are too crowded and saturated within this region. In total, the input catalogue contains 16 641 sources.

Fig. 2 shows an overview of the input catalogue used to extract and analyse the light curves: panels (a), (b), and (c) show the positions, the proper motions, and the colour–magnitude diagram (CMD) of the stars analysed in this work. We plotted in red the stars that have high probability to be 47 Tuc members, based on proper motions and parallaxes. We performed the 47 Tuc member selection as follows: first, in the vector point diagram (VPD) of panel (b), we selected by hand the stars that, on the basis of their proper motion, are candidate cluster members. We found the centre of the motion of the cluster by fitting single Gaussians to the $\mu_\alpha \cos\delta$ and μ_δ distributions of the selected stars, finding $(\mu_\alpha \cos\delta_0, \mu_\delta) = (5.2, -2.5)$ mas yr^{-1}. We selected all the stars within 3σ from the centre of the motion and for these stars we computed the median value of the parallax[2] $\pi = (0.24 \pm 0.06)$ mas: we considered candidate cluster members all the stars within $3\sigma_\pi$ from the median value of π. In the same way, we selected Small Magellanic Cloud (SMC) members considering all the stars within 3σ from the centre of the motion of the SMC $[(\mu_\alpha \cos\delta_0, \mu_\delta) = (0.5, -1.2)$ mas yr$^{-1}]$ and with parallaxes within 3σ from the median value $\pi = 0.03 \pm 0.07$ mas. The SMC high probable members are plotted in green in panels (a), (b), and (c) of Fig. 2.

We transformed the *Gaia* magnitudes of the stars in the input catalogue into *TESS* magnitudes using the relation $T - G$ versus $G_{BP} - G_{RP}$ illustrated in panel (d) of Fig. 2. To obtain this relation we cross-matched the *TESS* target list of the stars observed in the first seven sectors with Gaia DR2 catalogue. We considered all the stars with $G < 16$ and $T < 16$ and we fitted to the $T - G$ versus $B_P - R_P$ distribution a second-order polynomial [magenta line in panel (d) of Fig. 2]. We found:

$$T = G + a_0 + a_1 \times (G_{BP} - G_{RP}) + a_2 \times (G_{BP} - G_{RP})^2,$$

[2]Corrected for the offset tabulated by Riess et al. (2018)

where $a_0 = (0.014 \pm 0.004)$, $a_1 = (-0.643 \pm 0.007)$, and $a_2 = (0.055 \pm 0.003)$. Transformation from *Gaia* to *TESS* magnitudes is significant to minimize systematic residuals, during neighbour subtraction, due to colour terms.

2.3 Light curve extraction

For the extraction of the light curves from *TESS* images, we used an evolved, improved version of the code `img2lc` developed by Nardiello et al. (2015) and Nardiello et al. (2016a) for ground-based images and also adopted by Libralato et al. (2016a), Libralato et al. (2016b), and Nardiello et al. (2016b) for the extraction of light curves from *Kepler/K2* images of open clusters.

For each FFI, we transformed the (α, δ)-coordinates of the stars in the input catalogue in the image reference system using the WCS keywords and the distortion coefficients in the FITS header of the images. In particular we used the following equation to transform sky coordinates (α, δ) to geometric distortion corrected pixel coordinates (U, V) (Greisen & Calabretta 2002):

$$\begin{pmatrix} U \\ V \end{pmatrix} = CD^{-1} \begin{pmatrix} \alpha \\ \delta \end{pmatrix},$$

where `CD` is the transformation matrix that takes into account the rotation, scaling, and skew of the image. The `CD` elements are listed in the FITS header. Then, we transformed (U, V) in original pixel coordinates (x, y) using two inversion distortion polynomials, as described by Shupe et al. (2005):

$$x = U + \sum_{p,q} AP_{pq} U^p V^q$$

$$y = V + \sum_{p,q} BP_{pq} U^p V^q,$$

where `AP` and `BP` are the polynomial coefficients for the terms $U^p V^q$, and $p + q$ is the order of the polynomial. For all the FFIs analysed in this work $p + q = 4$.

For each image, we used the 200 brightest, unsaturated, and isolated stars in the input catalogue, to derive the photometric zero points between the calibrated *TESS* magnitude T_{cal} and the instrumental magnitude T_{inst}, $\Delta T = T_{cal} - T_{inst}$. In order to compute this quantity, we derived the instrumental magnitude of each star by

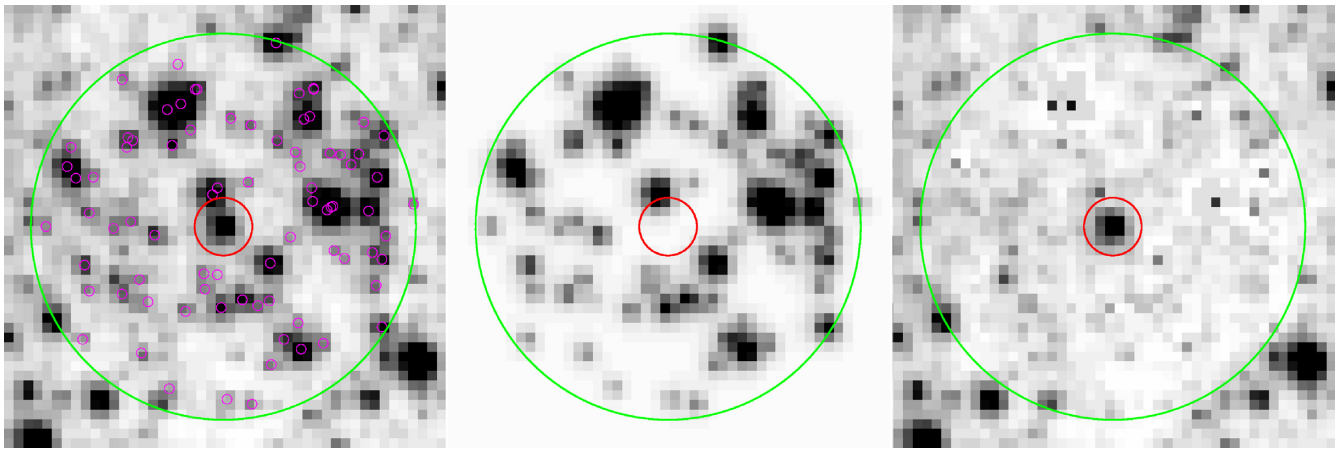

Figure 4. Procedure adopted for the subtraction of the neighbour stars of a target star in the input catalogue. Left-hand panel is one original FFI (`tess2018206192942-s0001-3-2-0120-s_ffic.fits`): red circle marks the target star (Gaia DR2 4689518492359359488), magenta circles are the neighbour stars in the input catalogue located within 20 pixels (green circle) from the target star. Middle panel is the image of the models of the neighbour stars, that will be subtracted from the original image, to obtain the right-hand panel.

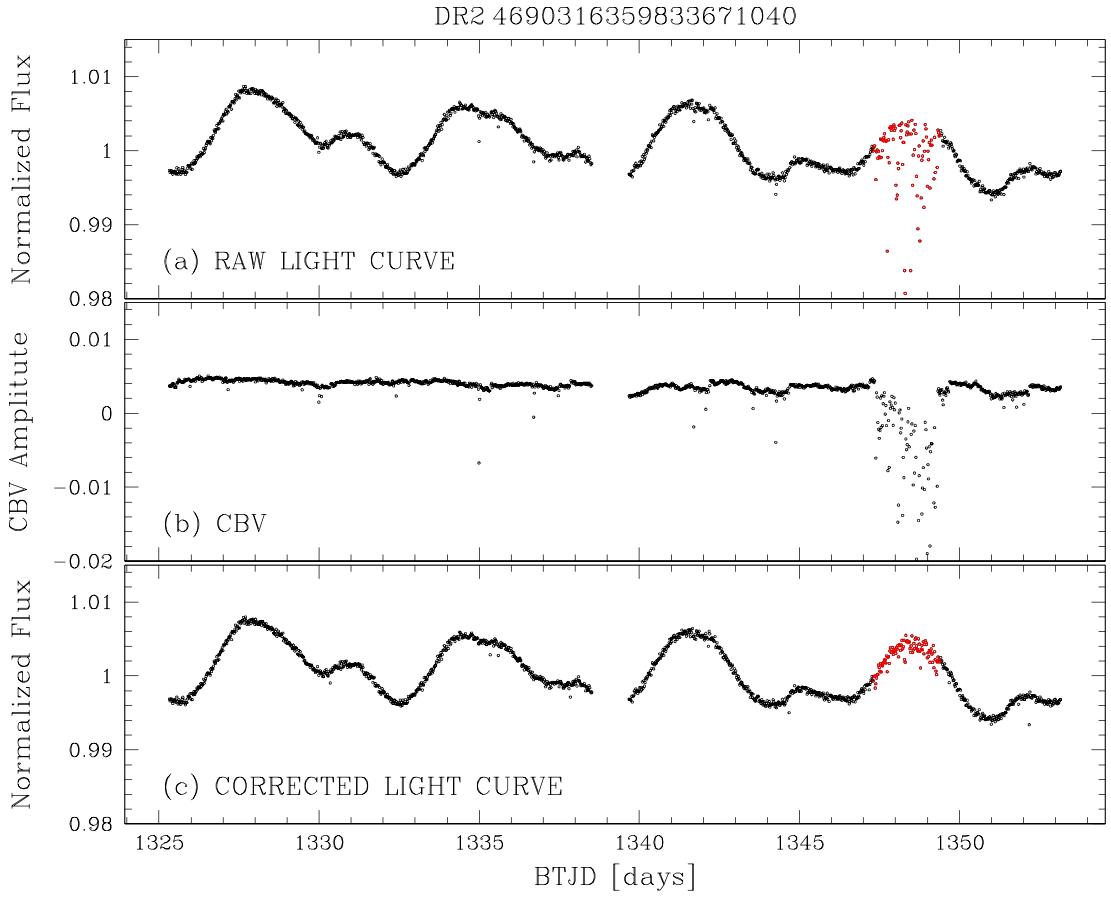

Figure 5. Procedure adopted for the correction of the light curve of the star Gaia DR2 4690316359833671040. Panel (a) shows the normalized raw light curve of the star obtained with 3-pixel aperture photometry; panel (b) is the CBV applied to the raw light curve to obtain the corrected light curve shown in panel (c). Red circles are the epochs for which the light curve shows larger systematic effects, due to a pointing problem occurred during the Sector-1.

fitting the local empirical PSF, and then we computed the average value of $T_{\rm cal} - T^i_{\rm inst}$, with $i = 1, ..., 200$. Fig. 3 shows the variation of ΔT during the Sector-1.

For each target star in the input list and for each image, the routine considered all the neighbour stars within a radius of 20 pixels and transformed their calibrated magnitudes in instrumental fluxes (e^-/s) using the previously calculated ΔT. Using the local PSF, the transformed fluxes and the positions, the software made a model of the neighbour stars and then subtracted it from the image. Finally it measured the target flux using both aperture and PSF-

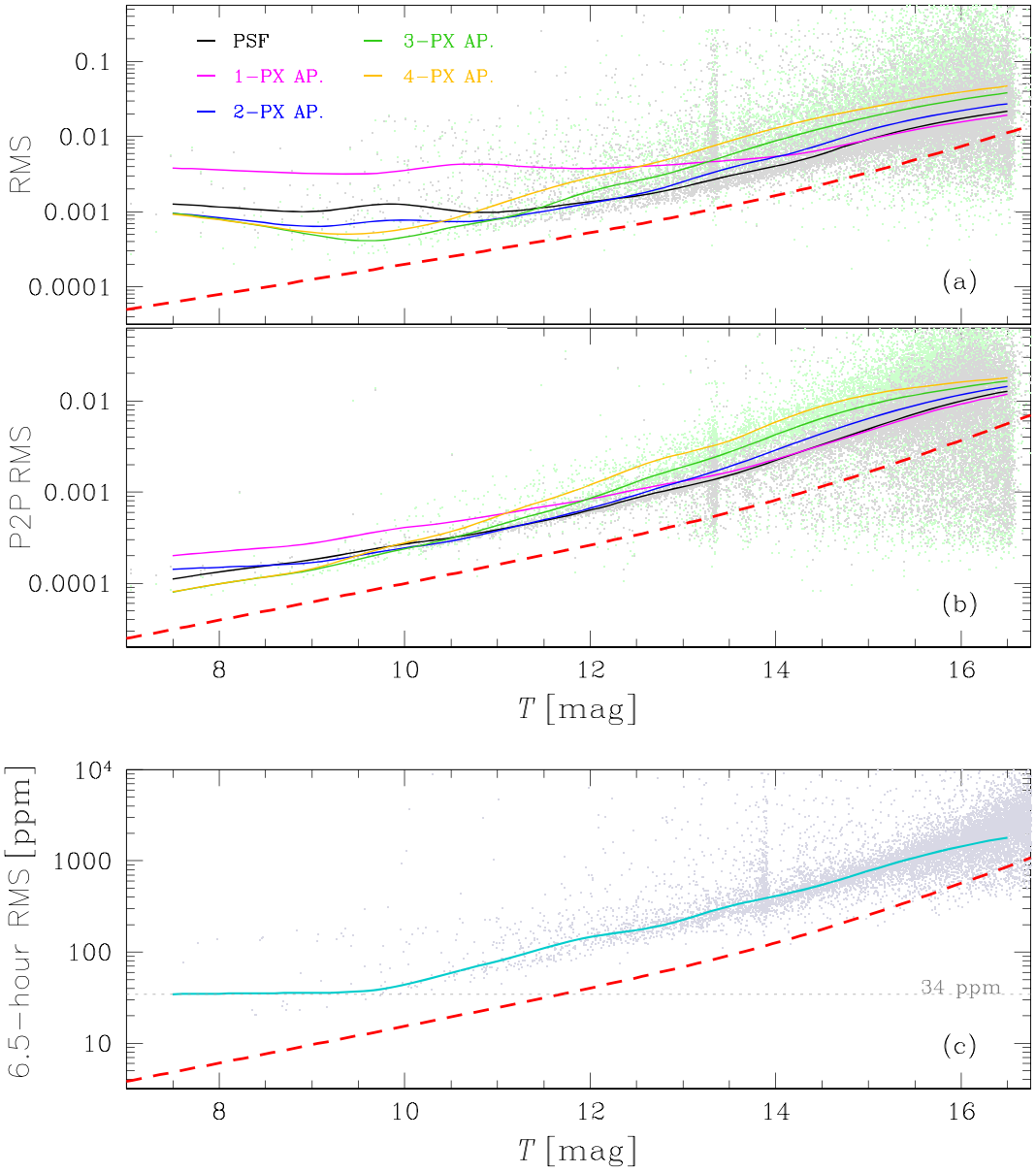

Figure 6. Photometric `RMS` (panel a), `P2P RMS` (panel b), and `6.5-h RMS` (panel c) as a function of the *TESS* magnitude. In panels (a) and (b), the solid lines represent the average trend of the two metrics for the different photometric methods: PSF-fitting (black), 1-pixel aperture (magenta), 2-pixel aperture (blue), 3-pixel aperture (green), and 4-pixel aperture (orange) photometries; light green and gray points are the distributions for the PSF-fitting and 3-pixel aperture photometries. Panel (c) shows the `6.5-h RMS` of the stars for which the best light curve has been chosen: azure line represents the average trend of the distribution; the red dashed line is the theoretical limit of the three RMSs (see the text for details).

fitting photometry on the neighbour-subtracted image. In the case of aperture photometry, we used four different aperture sizes: 1, 2, 3, and 4 pixel radius.

Fig. 4 shows the procedure for the subtraction of the neighbours from a single image. Left-hand panel shows a 45 × 45 pixel^2 subregion of a FFI centred on the target star. Middle panel is the same subregion with the models of the neighbours (located within a radius of 20 pixels from the target star) that are subtracted from the original image. Right-hand panel shows the region after the subtraction of the neighbours.

The fluxes, the epoch of the observations in TESS Barycentric Julian Day (BTJD), the positions on the images and the local sky values were stored in the related light curve file.

2.4 Systematic effects correction

The *TESS* light curves are affected by systematic artifacts, not correlated with the location and the luminosity of the stars on the CCD, but associated with spacecraft, detector and environment. Light curves of stars located on the same detector and observed in the same sector share common systematic trends, allowing us to model them using orthonormal functions, the so-called cotrending basis vectors (CBVs), and correct the systematics that affect the light curves applying to them the CBVs.

To extract the CBVs, we first computed the raw `RMS` for all the raw light curves and for all the photometric methods. To obtain the raw `RMS`, we iteratively computed the median value of the

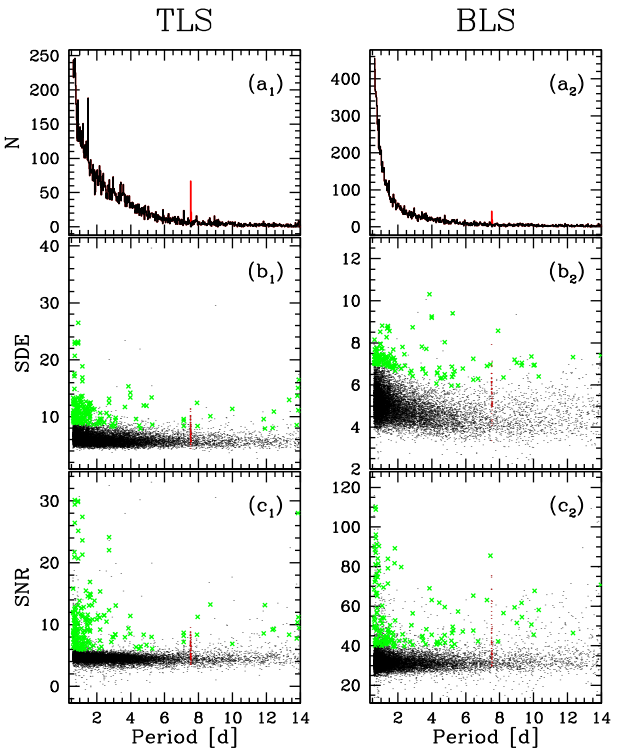

Figure 7. Overview on the selection of candidate transiting exoplanets adopted using TLS (left-hand panels) and BLS (right-hand panels) outputs. Panels (a) show the histogram of the best periods found using the different routines. Panels (b) are the SDE distributions as a function of the period, while panels (c) show the SNR distributions as function of the period. The red spike in panels (a) and the red points in panels (b) and (c) are the stars excluded in the spike suppression procedure. Green points are the stars that passed the selection criteria.

light curve and the value σ, defined as the 68.27th-percentile of the residual from the median, clipping-out at each iteration all the points above and below 3.5σ from the median value; after 10 iterations, we defined the RMS as the value of σ. For a given photometric method, we chose the magnitude interval where the light curves have, on average, lower raw RMS compared to the same light curves obtained with different photometric methods. In this magnitude interval we selected the light curves that showed an $RMS < RMS_{\rm median} + 2\sigma_{RMS}$, where $RMS_{\rm median}$ and σ_{RMS} are the median of RMS in the considered magnitude interval, and its standard deviation, respectively. Using these stars we extracted the CBVs using a principal component analysis. For each photometric method, we extracted 5 CBVs, that explain 85 per cent of the light curves' variance.

To correct the light curves, we developed a routine that finds the coefficients A_i that minimize the expression:

$$F^j_{\rm raw} - \sum_i (A_i \cdot {\rm CBV}^j_i), \quad (1)$$

where $F^j_{\rm raw}$ is the raw flux of the light curve at the epoch $j = 1, ..., 1282$, and $\rm CBV_i$ is the ith CBV, with $i = 1, ..., 5$. To minimize the expression (1), we used the Levenberg–Marquardt method (Moré, Garbow & Hillstrom 1980). We checked the final results changing the number of CBVs applied to the light curves, and we found that, on average, the application of just the first CBV produced light curves with the lowest RMS. In Fig. 5, we show the procedure adopted for the light curve correction applied to the star Gaia DR2 4690316359833671040 ($T \sim 10$). Panel (a) shows the 3-pixel aperture photometry: in red we highlighted the points of the light curves that show large systematic effects due to pointing problems occurred during the observations of the Sector-1;[3] panel (b) shows the CBV applied to the light curve of panel (a); panel (c) is the cotrended light curve. It is possible to note that the systematic artifacts due to the pointing problems are corrected.

2.5 Photometric precision

Panel (a) of Fig. 6 shows the RMS as a function of the *TESS* magnitude for all the stars for which we extracted the light curves. The RMS is computed using the cotrended light curves and adopting the procedure described in Section 2.4. For each photometric method, we divided the RMS distribution in bins of 0.75 T magnitude, and, within each bin, we calculated the 3.5σ-clipped average (with 10 iterations) of the RMS. We interpolated the mean RMS values with a cubic spline. We show in panel (a) of Fig. 6 the interpolated values with black, magenta, blue, green, and orange lines for PSF-fitting, 1-pixel, 2-pixel, 3-pixel, 4-pixel aperture photometries, respectively. The dashed red line is the theoretical RMS limit, obtained considering all the sources of noise (shot noise, sky, Readout Noise, and dark current), and adopting an average Readout Noise of $9\,{\rm e}^-$ pixel^{-1}, a dark current of $1\,e^-$ s^{-1} pixel^{-1},[4] an average sky value of $100\,{\rm e}^-$ s^{-1}, and an average aperture of 2 pixels. In the bright regime ($T \lesssim 10.5$) 3-pixel and 4-pixel aperture photometries give the lowest RMS; for stars with $10.5 \lesssim T < 13.5$ 2-pixel aperture photometry is the best photometry; in the faint regime 1-pixel and PSF-fitting photometry give the best results. For completeness, we plotted in grey and light green the RMS distributions for PSF-fitting and 3-pixel aperture photometries, respectively.

Because the simple RMS parameter is affected by the variability of the stars, we computed the point-to-point RMS (P2P RMS), defined as the 68.27th percentile of the distribution of the residuals from the median value of δF, where $\delta F_j = F_j - F_{j+1}$, and F_j and F_{j+1} are the flux values at the epoch j and $j + 1$, and $j = 1$, ..., 1281. We derived the mean trends of the P2P RMS distributions for the different photometric methods as done for the RMS. For the following analysis, we used these mean P2P RMS trends to identify, for each star, the best photometry: for each star in the input catalogue with a given T magnitude, we selected the light curve obtained with the photometric method that at the given T returns the lower mean P2P RMS. In this phase we also excluded all the light curves that have <300 photometric points and whose mean magnitude differs from that expected from the input catalogue >2 magnitudes.

Panel (c) of Fig. 6 shows the 6.5-h RMS distribution (gray points) for the previously selected light curves. This transit noise 6.5-h RMS is obtained as described by Gilliland et al. (2011), Gilliland et al. (2015), and Van Cleve et al. (2016): we flattened each light curve interpolating to it a 5th-order spline with 65 break points and removing out the outliers. We computed the standard deviation of a running mean with a window length equal to 6.5 h (13 points). The azure line in panel (c) is the mean trend of the 6.5-h RMS distribution, calculated as previously described: the trend reaches a minimum at ∼34 ppm. For $T < 10$, the distribution is bi-modal: stars that are not variable or whose period variability is >6.5 h have 6.5-h RMS ∼ 20 ppm. The stars with 6.5-h RMS

[3] https://archive.stsci.edu/tess/tess_drn.html
[4] As reported in the TESS Instrument Handbook.

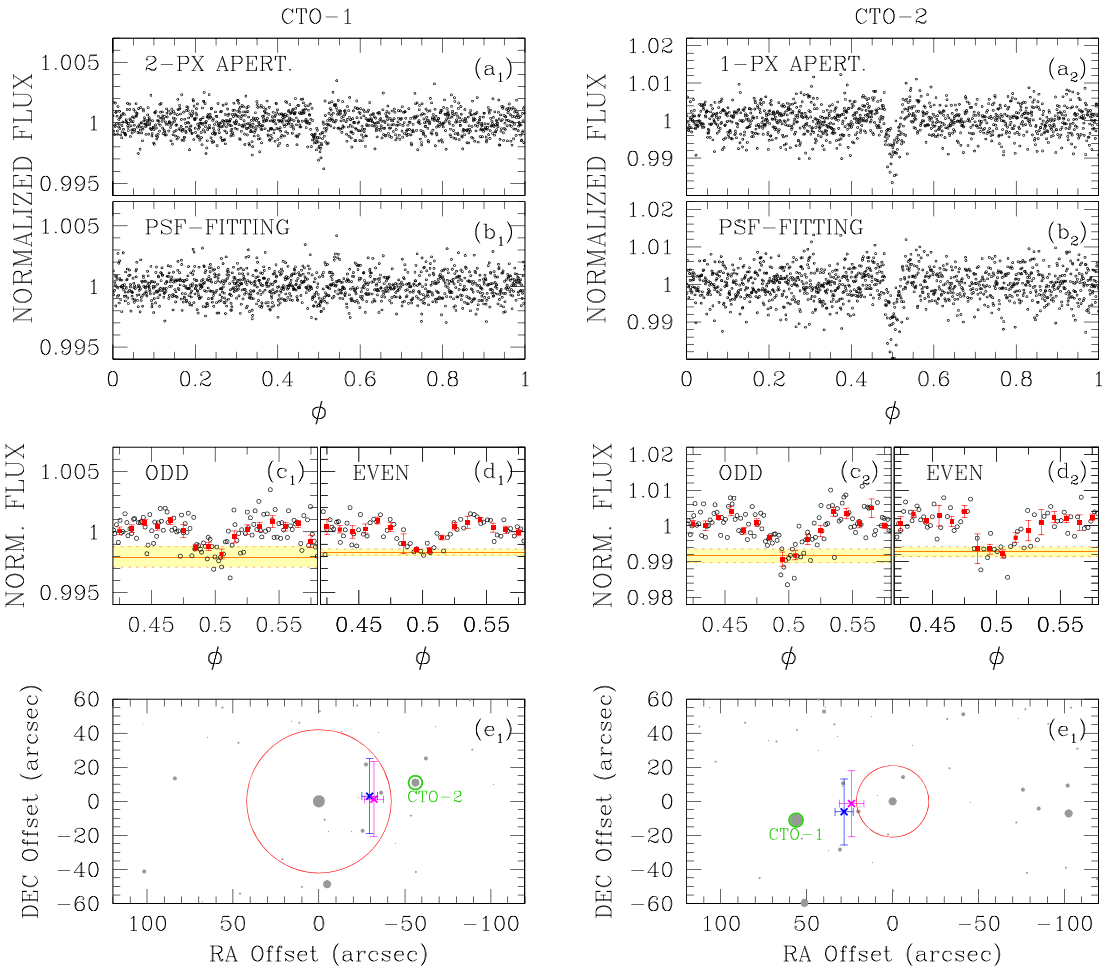

Figure 8. Procedure adopted for the vetting of the candidate exoplanets CTO-1 and CTO-2. Panels (a) show the best-photometry phased light curves for the two targets. Panels (b) are the phased light curves obtained with PSF-fitting photometry. Panels (c) and (d) plot the phased light curves for odd and even transits, respectively: orange horizontal lines represent the depth of the transits, in yellow the 1σ zone. Panels (e) show the centroid offsets calculated using the centroids from the out-of-transit image (magenta crosses) and the position from Gaia DR2 (blue crosses); the red circle is the photometric aperture adopted, gray circles are all the stars in the Gaia DR2 catalogue.

$\gtrsim 30$ are highly variable on short time-scales and the flattening is not perfect. For stars with $10 \lesssim T \lesssim 14$, we are able to detect exoplanets transits with depth <1 mmag, while for $T \gtrsim 14$ it is possible to find transits with depth <0.01 mag.

3 CANDIDATE EXOPLANET TRANSIT FINDING

We searched for transiting signals among the light curves selected in the previous section. As described in Section 2.5, we flattened all the light curves using 5th order splines defined on 65 knots. For each light curve, we removed out the outliers and the photometric points with $1347.4 < t_{\rm BTJD} < 1349.4$, whose photometry is affected by pointing problems and that, despite the cotrending, still have some residual systematic artifacts.

For each light curve, we extracted both the Box-fitting Least-Squares (BLS, Kovács, Zucker & Mazeh 2002) and Transit-fitting Least Squares (TLS, Hippke & Heller 2019) periodograms. For both techniques we searched for transiting objects having period $0.6 \leq P \leq 14$ d, and for each star we extracted the parameters useful to discriminate between light curves with and without candidate transits, such as the signal detection efficiency (SDE), the signal-to-noise ratio (SNR), the depth of the transit. To detect candidate transits we performed two independent analysis on BLS and TLS outputs and at the end we joined the results.

In Fig. 7, we summarize the procedure adopted for the selection of candidate transiting exoplanets both for TLS (left-hand panels) and BLS (right-hand panels) technique. As described in Nardiello et al. (2015), we excluded spurious periods due to systematic errors by constructing the histogram of the period and removing the stars that form the spikes in the histogram: the red spike (∼7.5 d) in panels (a_1) and (a_2) represents the stars we removed. In a second step, we divided the distributions of SDE (SNR) in period intervals $\delta P = 0.5$ d and, within each bin, we calculated the 3σ-clipped mean value of SDE (SNR), $\overline{\rm SDE}$ ($\overline{\rm SNR}$), and its standard deviation $\sigma_{\rm SDE}$ ($\sigma_{\rm SNR}$). We interpolated the mean points with a spline and we saved all the stars with SDE $> \overline{\rm SDE} + 3 \times \sigma_{\rm SDE}$ and SNR $> \overline{\rm SNR} + 3 \times \sigma_{\rm SNR}$. We excluded all the stars having transit depths >5 per cent. In panels (b) and (c) the stars that passed the selection criteria are plotted in green: we recovered 186 stars and 145 stars in the case of TLS and BLS, respectively, with 63 stars in common.

Finally, we visually inspected the candidate transits that passed the selections to exclude false alarms. We found seven interesting

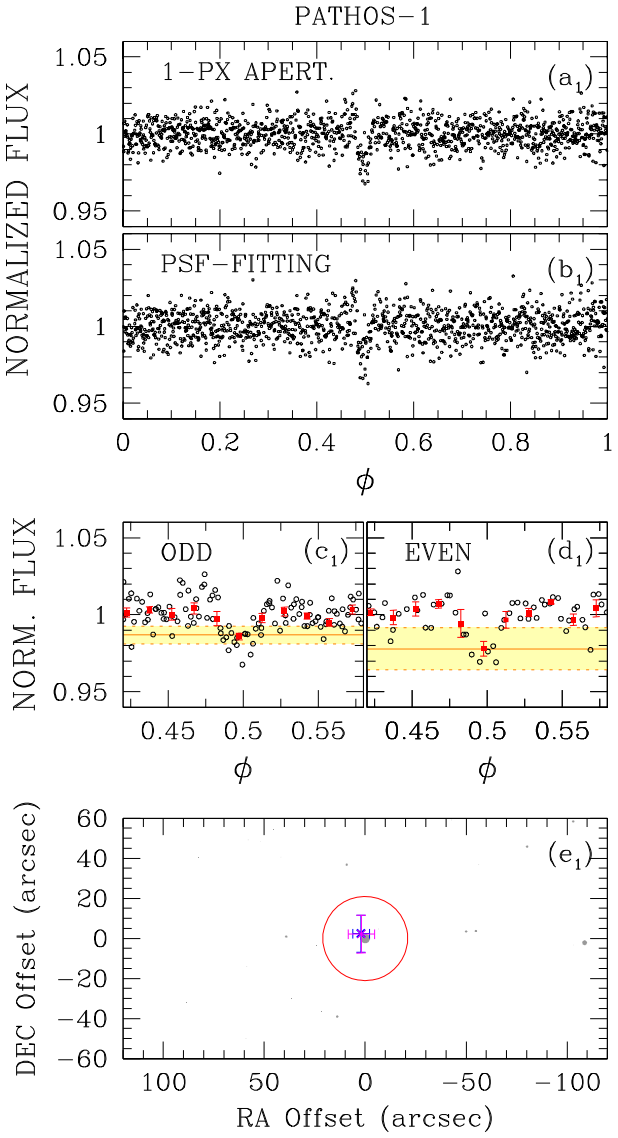

Figure 9. As in Fig. 8, but for PATHOS-1.

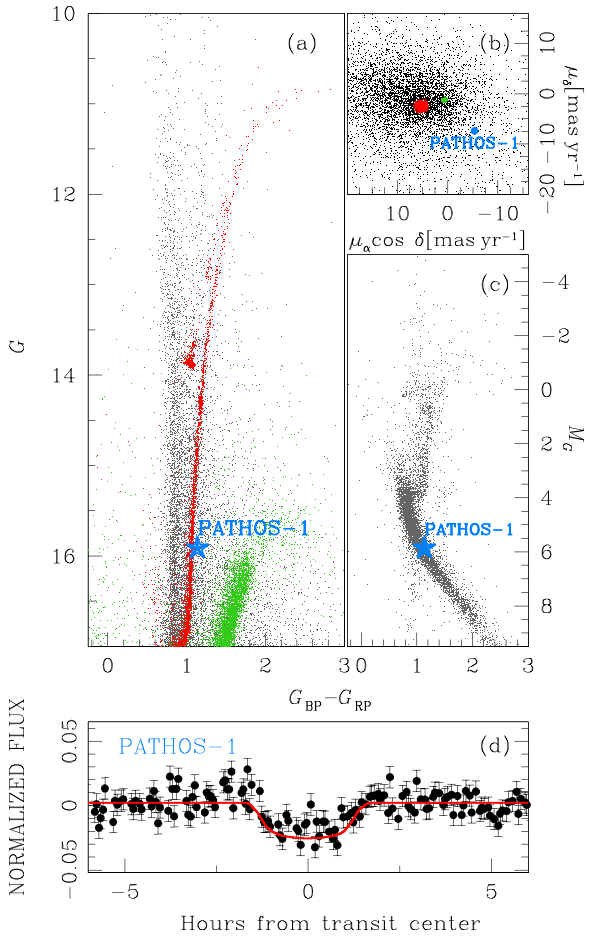

Figure 10. Panel (a) shows the G versus $G_{\rm BP} - G_{\rm RP}$ CMD: in red are the stars that have high probability to be 47 Tuc members, in green the stars with high probability to belong to the SMC, in gray the field stars of the Milky Way. Panel (b) is the VPD for 47 Tuc, SMC, and Milky Way stars plotted in red, green and gray, respectively. Panel (c) shows the absolute magnitude $M_{\rm G}$ versus $G_{\rm BP} - G_{\rm RP}$ CMD for the Milky Way stars. In all the panels, the position of the candidate exoplanet PATHOS-1 is shown in azure. Panel (d) is the phased light curve of PATHOS-1; in red the best-fitting model (see text for details).

objects on which we performed a series of tests to confirm or exclude the planetary nature.

3.1 Neighbour contamination

As a first test, we checked if the candidates are contaminated by close stars. We considered all the stars within the input catalogue that are at a distance <100 arcsec ($\lesssim$5 pixels) from the target candidate and we checked their periods and phased light curves. In this way we excluded four stars that are blended with close eclipsing binaries.

Among the 3 stars that succeed the check, two of them are close stars showing the same (interesting) signal. We will analyse all of them in the next section.

3.2 Vetting and modelling of the candidates

In this section, we verified that the selected stars are well-behaved candidate transiting exoplanets. In order to do this, we did the following tests: (i) we checked the position of the centroid of the star during and outside the transit events; (ii) we compared the depth of

Table 1. Transit parameters for the candidate exoplanet.

PATHOS-1	
Gaia DR 2 ID	4702085154340085248
$\alpha_{\rm J2000}$ (°)	2.879 651 46
$\delta_{\rm J2000}$ (°)	−70.986 935 22
T (mag)	15.3
$R_\star$ ($R_\odot$)	0.86 ± 0.02
$M_\star$ ($M_\odot$)	0.78 ± 0.02
$\rho_\star$ ($\rho_\odot$)	$1.24^{+0.07}_{-0.06}$
Period (d)	$3.8582^{+0.0017}_{-0.0014}$
T_0 (BTJD)	1339.677 ± 0.003
$R_{\rm p}/R_\star$	$0.152^{+0.011}_{-0.009}$
$R_{\rm p}$ ($R_{\rm Jup}$)	$1.27^{+0.10}_{-0.07}$
$a/R_\star$	$11.11^{+0.17}_{-0.22}$
i (°)	$89.2^{+0.8}_{-0.5}$
T_{14} (min)	181^{+5}_{-4}
$u1$	0.42 ± 0.10
$u2$	0.18 ± 0.10

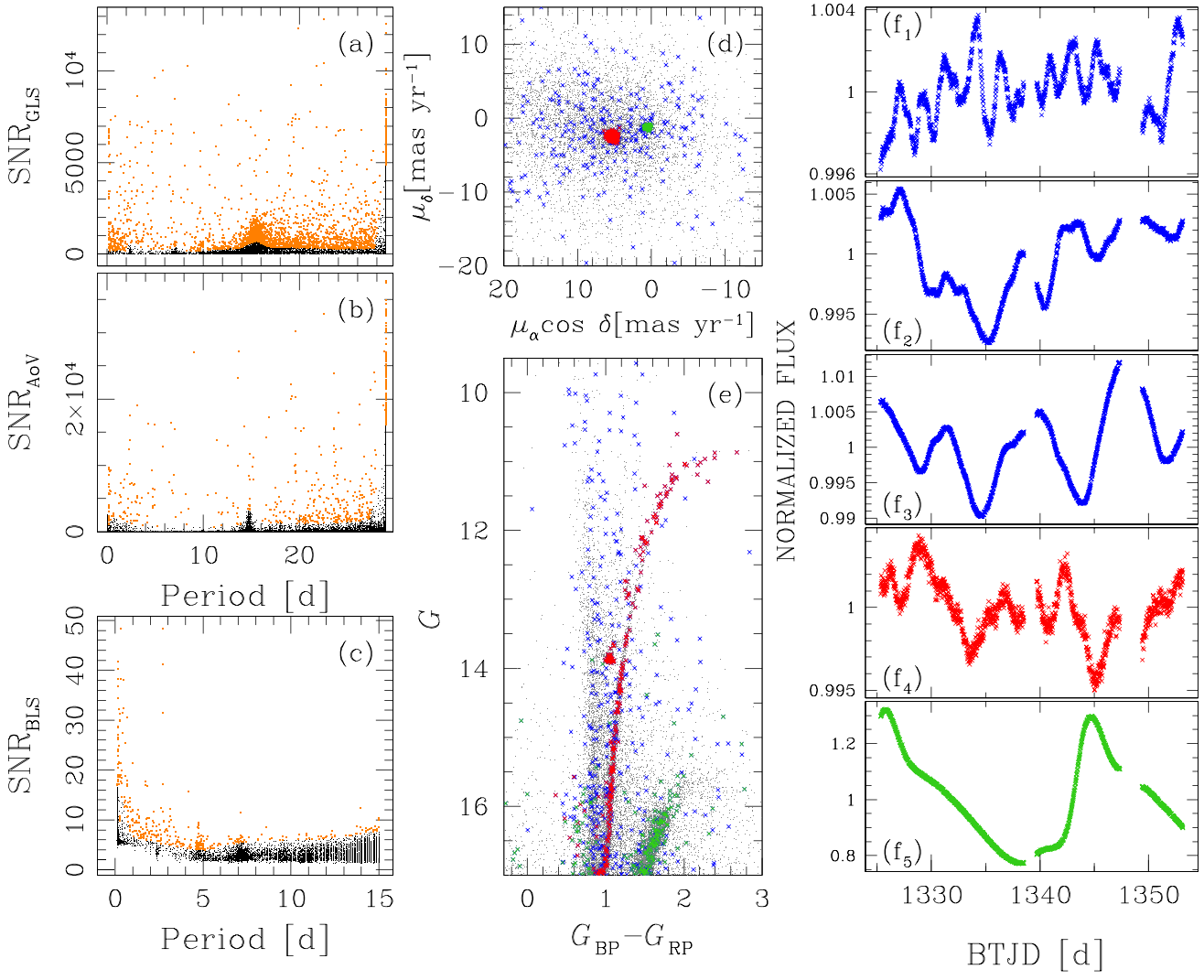

Figure 11. Procedure adopted for the selection of candidate variable stars. Panels (a), (b), and (c) show the selection in the SNR versus Period plane for the GLS, AoV, and BLS periodograms, respectively: in orange are the stars that have high probability to be variables. Panels (d) and (e) are the VPD and the G versus $G_{BP} - G_{RP}$ CMD, respectively: in blue, red, and green are the candidate variable stars that belong to field, 47 Tuc, and SMC, respectively. Panels (f) are some examples of light curves of stars with high probability to be variables: the light curves are colour-coded as in panel (d) and (e).

the odd and even transits; (iii) we compared the best photometry with that obtained using PSF-fitting, less affected by the contamination effects. The following sections will be dedicated to the vetting of the candidate transiting objects (CTOs).

3.2.1 Two close candidates

The first two candidates are two close stars at a distance $\delta r \simeq 57.2$ arcsec, and show similar signals in their light curves. The brighter star (Gaia DR2 4689801887175745536, hereafter CTO-1) has $T \sim 12.2$ and, as explained in Section 2.5, the best light curve is obtained using the 2-pixel aperture photometry. The fainter star (Gaia DR2 4689813608144062080, hereafter CTO-2) has $T \sim 14.3$, and 1-pixel aperture photometry gives the best result. The two stars present a periodic transit event with period $P \sim 3.982$ d, but different depth: for CTO-1, the transit depth is ∼0.2 per cent [panel (a_1) of Fig. 8], while for CTO-2 the transit is ∼four times deeper, as shown in panel (a_2) of Fig. 8.

To verify if the signal belongs to CTO-1 or CTO-2, for both the targets we compared the best-aperture photometry with the PSF-fitting photometry [panels (b) of Fig. 8], that is less affected by contamination problems. As shown in panel (b_1) of Fig. 8, even if the scatter of the PSF-fitting light curve of CTO-1 is similar to that of 2-pixel aperture photometry [σ(PSF) ∼ 1060 ppm versus σ(APER) ∼ 970 ppm], the PSF-fitting photometry shows a less evident transit, with depth ∼0.1 per cent. On the other hand, comparing the PSF-fitting [panel (b_2)] and 1-pixel aperture [panel (a_2)] photometries of CTO-2, it is possible to confirm the presence of the transits in both light curves, with the same depth.

As shown in Fig. 8, we compared the depth of odd [panels (c)] and even [panels (d)] transits, to exclude the hypothesis that the transits events are eclipses of an eclipsing binary. We calculated the mean depth of odd/even transits [orange continuous lines in panels (c)] and its standard deviation (yellow strips): for CTO-1, we found that the odd and even transits have a depth of 2.1 ± 0.8 mmag and 1.6 ± 0.3 mmag, respectively; CTO-2 have odd and even transits

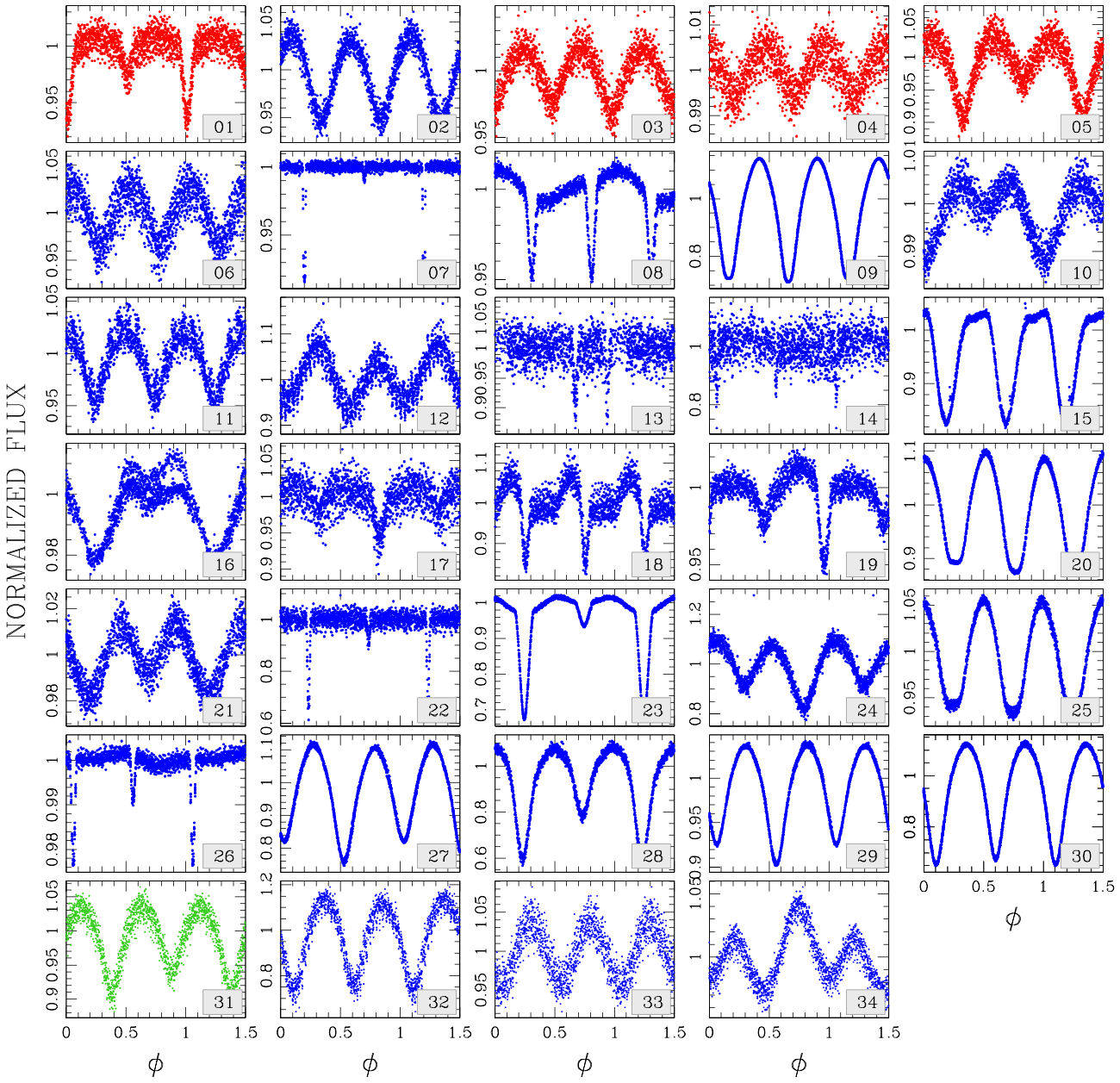

Figure 12. Light curves of eclipsing binaries found in the field analysed in this work. Light curves are colour-coded as in Fig. 11.

depth of 8.3 ± 1.9 mmag and 7.2 ± 1.3 mmag. For both stars, the depth of odd and even transits overlaps within $1\times\sigma$.

We analysed the centroid offset using the technique described by Twicken et al. (2018). Briefly, we selected the images corresponding to the in-of-transit events and the images near the transit events (out-of-transit). For each transit, we calculated the mean in- and out-of-transit images, and then we stacked together all the mean in- and out-of-transit images. We calculated the difference image subtracting pixel-by-pixel the in-of-transit stack to the out-of-transit stack. We calculated the photocentres on the out-of-transit and on the difference images. We calculated two offsets: (1) the difference between the centroid obtained from the out-of-transit and the difference images, and (2) the difference between the Gaia DR2 position and the centroid from the difference image. The offset locates the source of the transit signature.

Panels (e) of Fig. 8 show the out-of-transit centroid analysis for the two stars. In each panel, the target star is centred in (0,0) and the red circle is the photometric aperture used to extract the light curve; in gray are all the sources in the Gaia DR2 catalogue, and magenta and blue crosses are the centroid offsets calculated using the centroids from the out-of-transit image and the position from Gaia DR2, respectively. According to the centroids, the transit events do not occurs on CTO-1 or CTO-2, but to a very faint star ($G > 17.2$) between the two candidates.

We searched in literature whether already discovered eclipsing binaries with magnitude $G > 17$ are located in that sky regions: Pawlak et al. (2016), in a study of eclipsing binaries in the Magellanic Clouds using OGLE data (Udalski et al. 1992), found an eclipsing binary (OGLE-SMC-ECL-6193) with period $P \sim 7.9733$, so twice the period of the two candidates, $G \sim 17.25$ and located exactly where the centroids are shown in panels (e)

Table 2. List of eclipsing binaries.

# EB	α (J2000) (°)	δ (J2000) (°)	Gaia DR 2 ID	T	G	G_{BP}	G_{RP}	$\mu_\alpha \cos\delta$ (mas yr^{-1})	μ_δ (mas yr^{-1})	P (d)	Note	Ref.
01	6.537 000 594	−72.117 086 89	4689629611756844672	15.65	15.84	15.95	15.59	5.267	− 1.957	1.150 726	V46, 0063	(1,2)
02	5.697 991 131	−72.221 453 20	4689625041910756480	15.11	15.53	15.84	15.04	11.575	− 1.031	0.278 849	V50	(1)
03	6.543 979 192	−72.185 504 01	4689628203007617792	16.17	16.46	16.52	15.98	5.660	− 2.563	0.378 792	V45, 6257	(1,2)
04	5.825 314 808	−72.311 584 97	4689619853590073216	13.33	13.88	14.34	13.26	5.802	− 2.943	0.383 336	V49	(1)
05	6.679 190 520	−72.255 768 87	4689579961931616640	16.38	16.72	16.93	16.29	5.911	− 2.183	0.446 193	V53, 6261	(1,2)
06	6.749 464 138	−71.919 389 68	4689646757262208000	15.43	15.88	16.01	15.16	7.993	2.603	0.347 537	KalE1	(1)
07	5.413 085 792	−72.520 899 53	4689547010942141056	13.47	14.00	14.42	13.41	9.254	− 10.723	5.227 904		
08	6.355 276 472	−72.549 857 87	4689552783378799744	13.75	14.41	14.96	13.66	12.478	6.540	0.677 519	0057	(2)
09	4.340 046 990	−71.915 835 31	4689821167286415744	9.74	10.02	10.25	9.71	29.282	− 10.217	0.594 934	AQ Tuc	(3)
10	3.926 140 119	−72.404 555 59	4689606693809057920	12.52	12.85	13.08	12.47	12.182	0.874	4.183 775		
11	5.617 000 506	−71.355 972 97	4689919401777839872	15.25	15.57	15.80	15.19	2.629	− 2.465	0.271 553	6237	(2)
12	4.438 502 576	−71.473 518 63	4689892051426793088	15.93	16.64	17.27	15.85	1.607	2.576	0.301 928	6202	(2)
13	8.383 993 384	−72.443 714 08	4689170393848047616	16.37	16.34	16.29	16.28	− 2.151	− 0.490	9.700 781	0190	(2)
14	8.667 676 514	−72.420 935 51	4689175444729490176	16.09	16.58	16.96	16.02	7.916	− 2.849	6.348 956	6320	(2)
15	3.233 508 991	−72.317 015 94	4689705065728365952	13.87	14.58	15.23	13.80	14.594	− 11.702	6.221 432		
16	8.890 463 344	−72.004 247 10	4689948607555229440	13.31	14.00	14.62	13.25	21.512	− 7.481	8.311 906		
17	9.001 923 031	−72.136 926 03	4689195235938665984	16.49	16.95	17.30	16.42	10.471	− 0.916	2.195 023		
18	3.106 567 298	−71.636 967 59	4701807184057132544	15.34	16.07	16.76	15.26	19.053	− 9.645	0.797 952		
19	7.236 826 679	−73.047 335 69	4688719937672536576	15.52	16.02	16.39	15.44	9.457	1.928	0.887 469	0110	(2)
20	6.095 619 143	−71.048 398 47	4701937201307042304	10.84	11.28	11.58	10.75	− 9.681	− 32.364	0.337 970		
21	8.348 316 851	−71.266 297 84	4690231525639747072	5.84	6.04	6.22	5.83	73.596	− 12.372	7.108 649	Theta Tuc	(3)
22	4.674 966 177	−71.024 741 37	4701931566310065280	16.15	16.73	17.19	16.06	17.406	1.644	3.666 514	6209	(2)
23	2.505 425 028	−71.589 024 03	4701817938655245568	10.51	10.77	10.95	10.48	2.737	3.244	2.727 260		
24	9.268 095 200	−71.434 385 59	4690047048205684736	15.86	16.11	16.27	15.80	4.118	4.035	0.462 172	0301	(2)
25	2.113 365 648	−72.312 074 17	4689760969022718720	13.08	13.49	13.79	13.02	− 0.194	0.552	0.330 047	6174	(2)
26	4.262 175 365	−70.991 499 06	4701976680646546688	11.58	12.16	12.65	11.52	15.144	− 10.681	1.406 333		
27	2.826 367 562	−71.300 141 65	4701877209203898368	13.83	14.37	14.83	13.76	− 12.364	− 6.930	0.269 175	6181	
28	4.266 066 198	−70.912 469 27	4701989595612092416	15.96	16.92	18.00	15.88	6.717	− 7.449	0.302 563		
29	5.461 765 066	−70.778 518 42	4702006058222771072	12.30	12.82	13.27	12.25	11.954	− 7.653	0.271 736		
30	2.157 617 319	−71.487 422 90	4701865698691623680	13.59	14.03	14.39	13.54	2.934	1.175	0.305 206	6175	(2)
31	7.088 826 924	−73.391 198 41	4688521407109977344	15.68	16.48	17.28	15.61	0.379	− 1.267	1.705 885		
32	5.850 347 702	−73.532 129 06	4688493335202967680	16.44	16.84	17.10	16.34	0.714	− 4.793	0.385 427	0024	(2)
33	2.534 043 926	−71.118 176 83	4701889887947453824	15.58	16.01	16.34	15.51	19.158	− 8.877	0.177 335		
34	3.200 471 157	−73.299 415 28	4688666370837766144	14.62	14.92	15.12	14.56	2.890	− 10.635	1.917 045		

Note. References (1) Clement et al. (2001, updated to 2017); (2) Pawlak et al. (2016); (3) Samus' et al. (2017).

of Fig. 8. The depth of the primary eclipses is ∼0.3 mag, while that of the secondary eclipses is ∼0.2 . So, given the differences in magnitudes between the two candidates and the eclipsing binary and the fraction of light of the eclipsing binary that falls within the aperture of the two candidates, we expect an induced transit of depth ∼0.1 per cent and ∼1 per cent for CTO-1 and CTO-2, respectively.

We conclude that the two candidates are false positive generated by the blending with a fainter eclipsing binary located between them.

3.2.2 *A candidate exoplanet: PATHOS-1*

Fig. 9 shows the vetting procedure for the candidate transiting exoplanet PATHOS-1 ($T \sim 15.3$, $P \sim 3.86$ d). The comparison between the best photometry (1-pixel aperture, panel (a_1)) and the PSF-fitting photometry shows that it is possible to identify the transit events in both of the light curves. Comparing the odd (1.3 ± 0.6 per cent) and even (2.2 ± 1.3 per cent) transit events [panels (c_1) and (d_1)] we found that the depths are compatible within $1\times\sigma$. From the analysis of out-of-transit centroids [panel (e_1) of Fig. 9], we confirm that the transit events occur on PATHOS-1.

PATHOS-1 is a field star located on the main sequence (MS) of the Galaxy [see panels (a), (b), and (c) of Fig. 10].

We extracted transit parameters using a modified version of the code used by Borsato et al. (2019) and Benatti et al. (2019). It selects a portion of the light curve around each transit of about $\pm 2 \times T_{14}$ (T_{14} is the duration of the transit from the TLS) from the linear ephemeris determined with TLS. This code models the transit with the batman-package (Kreidberg 2015) and computes the posterior distribution with `emcee` (affine invariant Markov-Chain Monte Carlo sampler; Foreman-Mackey et al. 2013).

The code fits as common parameters the stellar density $\rho_\star$ (in Solar unit), the base-2 logarithm of the period of the planet ($\log_2 P$), the radii ratio ($k = R_p/R_\star$), the impact parameter (b), the quadratic limb darkening (LD) parameters, q_1 and q_2, as proposed by Kipping (2013), a base-2 logarithm of a jitter term ($\log_2\sigma_j$), the reference transit times (T_0). For each transit, it fits a detrending polynomial of third order (coefficients c_0, c_1, c_2) and the time of the centre of the transit (TT). It this way it computes simultaneously each transit time (TT) and the linear ephemeris (given by the period and T_0). We fixed the eccentricity e to 0 and the argument of the pericenter ω to 90 deg. We used uniform-uninformative priors within conservative boundaries for all the parameters, but Gaussian priors for the stellar density and LD parameters. The prior for the density has been computed from the stellar radius ($R_\star$) and mass ($M_\star$); from the Gaia DR2 catalogue the star has $R_\star = 0.86 \pm 0.02\,R_\odot$ and, using mass–luminosity relation $L \propto M^{3.5}$, we found $M_\star = 0.78 \pm 0.02\,M_\odot$. The quadratic LD

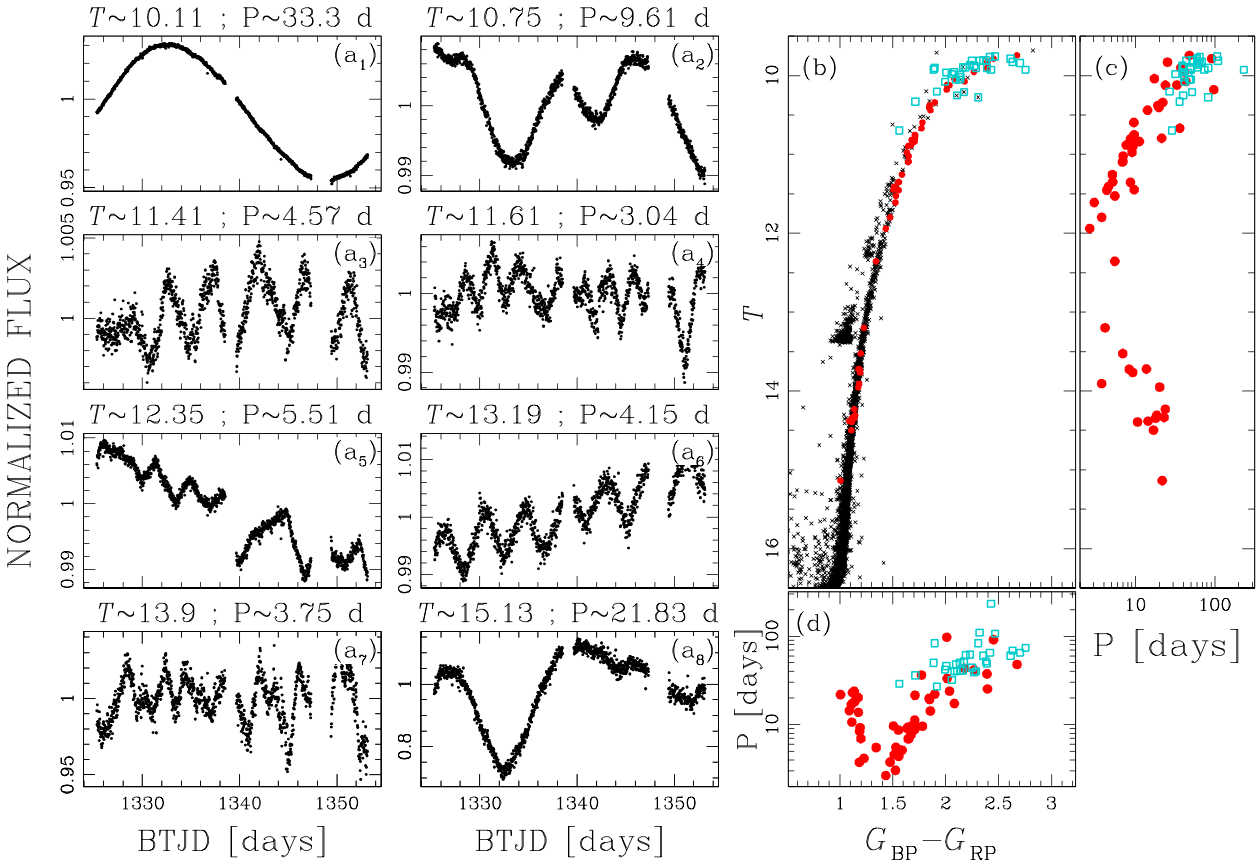

Figure 13. Analysis of RGB stars. Panels (a_1)–(a_8) show a sample of light curves of RGB stars, ordered by magnitude. Panel (b) shows T versus $G_{BP} - G_{RP}$ CMD; panels (c) and (d) are the PL and the PC relations. In panels (b), (c), and (d) azure squares are determined by Lebzelter et al. (2005), red points are obtained in this work.

parameters have been determined from the Claret (2018) table for $T_{eff} = 4985 \pm 59$ K (from Gaia DR2) and we adopted priors with a Gaussian conservative error of about 0.1 for both the parameters.

We run `emcee` with 72 walkers and for 20 000 steps. We removed the first 2000 steps as burn-in (checked visually the convergence of the chains) and we used a pessimistic thinning factor of 100. From the posterior distribution we computed the physical posteriors and computed the uncertainties as the high-density interval (HDI) at 68 per cent (1σ equivalent). We computed the median of the physical posterior distribution as the best-fitting transit parameters (reduced $\chi^2 \sim 0.92$). We found that the period of the candidate exoplanet is $P \sim 3.8582$ d and $k \sim 0.152$, i.e. $R_p \sim 1.27\,R_{Jup}$. Table 1 gives all the physical parameters with errors.

Panel (d) of Fig. 10 shows the phased light curve and, overimposed in red, the best-fitting model.

4 VARIABLE STARS

Variable star detection has been performed using three different algorithms: the Generalized Lomb-Scargle (GLS) periodogram (Zechmeister & Kürster 2009), the Analysis of Variance (AoV) periodogram (Schwarzenberg-Czerny 1989), and the BLS periodogram. The procedure is illustrated in Fig. 11. We isolated the candidate variable stars using the SNR parameter and adopting the procedure described in Nardiello et al. (2015): first, we produced the histograms of the detected periods for all the light curves and suppressed the spikes due to systematic effects in the light curves. We divided the SNR distributions in bins of period $\delta P = 1$ d and we computed the 3.5σ-clipped mean and standard deviation values of the SNR within each period interval. We interpolated the points 4σ above the mean values with a spline and selected all the stars above this line [orange points in panels (a), (b), and (c) of Fig. 11]. The number of candidate variable stars so selected are 2446 and 561 according the GLS and AoV algorithms, respectively. The variables identified by both the techniques are 502. The number of variable sources found with BLS periodogram is 391. We used a routine of `VARTOOLS` (Hartman & Bakos 2016) to exclude the sources that show variability because blended with a real variable star. After excluding blends and after a visual inspection, we identified 34 eclipsing binaries. Positions of the candidate variables in the VPD and CMD are plotted in blue (field stars), red (47 Tuc members), and green (SMC stars) in panels (d) and (e) of Fig. 11, respectively. Panels (f) show some examples of variable stars, colour-coded as in panels (d) and (e). The magnitude of these stars spans from $T \sim 7.4$ to $T \sim 13.4$.

4.1 Eclipsing binaries

We detected 34 eclipsing binaries. Their phased light curves are shown in Fig. 12 colour-coded as the variables in Fig. 11. Among the detected eclipsing binaries, 4 of them have a high probability to be 47 Tuc members (in red), one is a star in the SMC (in green), and the other 28 stars belong to the Galactic field (in blue). In

Table 3. List of the analysed RGB stars in 47 Tuc.

α (J2000) (°)	δ (J2000) (°)	Gaia DR 2 ID	T	G	G_{BP}	G_{RP}	P (d)	σ_P (d)
		RGB						
6.429 20058	−72.068 215 14	4689627069134206080	13.72	14.32	14.82	13.65	13.76	0.10
6.436 62601	−72.087 781 19	4689627000414752896	14.31	14.89	15.38	14.23	18.62	0.26
5.668 59934	−72.148 572 13	4689637407107299840	10.97	11.76	12.55	10.91	9.08	0.13
6.018 83235	−71.953 100 74	4689644730042501760	10.60	11.43	12.32	10.54	9.59	0.06
6.121 40329	−72.206 475 51	4689623010398337408	13.95	14.54	15.05	13.88	20.27	0.21
5.648 47070	−72.022 814 11	4689642698537939328	13.72	14.32	14.84	13.65	8.37	0.11
6.433 20055	−72.114 105 71	4689626725536883328	9.95	10.96	12.17	9.90	41.55	–
6.449 80872	−72.089 721 15	4689626794256322048	14.39	14.96	15.42	14.31	10.65	0.17
6.453 52017	−72.088 554 92	4689626794256321024	14.35	14.92	15.36	14.23	18.00	0.18
6.411 09649	−72.018 353 33	4689639919678548736	11.41	12.15	12.82	11.31	4.58	0.02
5.596 06753	−72.118 078 31	4689638373492005888	10.75	11.56	12.40	10.69	9.66	0.14
6.378 38253	−71.999 104 31	4689640194556564224	14.38	14.94	15.39	14.30	14.44	0.12
5.574 56597	−72.103 433 71	4689638442211439872	10.12	11.04	12.08	10.07	33.31	–
6.357 01402	−72.177 603 43	4689623289563167360	10.12	11.05	12.11	10.07	23.89	0.34
6.498 58087	−72.075 269 96	4689632875931941888	11.02	11.81	12.61	10.96	7.02	0.07
6.489 73686	−72.131 336 62	4689629371238695552	11.61	12.35	13.07	11.55	3.04	0.01
6.511 60277	−72.055 078 97	4689632974708827776	13.20	13.82	14.36	13.13	4.16	0.03
6.343 67313	−72.198 705 24	4689622460621134720	11.35	12.11	12.85	11.29	8.67	0.15
5.835 24393	−71.938 833 81	4689831200329811840	14.50	15.06	15.53	14.43	16.91	0.24
5.523 87023	−72.065 726 26	4689618273040536704	10.67	11.50	12.38	10.61	36.33	–
5.649 34543	−72.186 486 47	4689625282428885120	9.78	10.84	12.21	9.76	91.28	–
6.031 88484	−71.926 107 41	4689645004920347264	15.14	15.65	16.07	15.06	21.84	0.38
6.217 01197	−71.936 457 39	4689644420804776960	9.90	10.94	12.25	9.865	37.41	–
6.216 56039	−72.227 292 00	4689622052612663680	14.23	14.81	15.29	14.16	23.82	0.42
6.315 62558	−72.212 359 71	4689622430569760640	10.89	11.68	12.48	10.83	9.34	0.07
5.524 69338	−72.130 274 78	4689614901478662272	10.40	11.27	12.19	10.34	19.83	0.12
6.052 34523	−71.921 071 73	4689645107999550720	11.80	12.52	13.21	11.73	3.77	0.03
6.455 10154	−72.194 218 79	4689622396209979136	14.34	14.91	15.37	14.25	23.03	1.14
6.283 43260	−71.926 325 78	4689644352084823936	13.77	14.37	14.89	13.70	9.25	0.09
5.982 79786	−71.904 909 59	4689832712158218880	12.36	13.02	13.64	12.29	5.51	0.05
6.516 17594	−71.975 136 01	4689645898275596288	13.53	14.13	14.66	13.46	6.95	0.06
5.715 71955	−72.243 800 77	4689624212967816064	11.09	11.88	12.67	11.02	6.96	0.05
6.093 69763	−71.891 298 82	4689832849597140096	9.83	10.87	12.19	9.79	25.36	2.28
6.400 41875	−72.237 508 38	4689575289007212416	11.45	12.18	12.89	11.38	9.65	0.08
5.913 28145	−72.277 757 11	4689620334626390784	10.38	11.24	12.17	10.32	19.23	0.03
5.396 19011	−71.999 718 00	4689807354671547648	10.04	10.98	12.08	9.99	17.35	0.28
5.574 86258	−72.261 691 93	4689600680854700288	10.79	11.61	12.44	10.73	21.47	0.21
5.682 79610	−71.875 482 64	4689835082980178304	11.94	12.65	13.31	11.88	2.66	0.01
6.761 44736	−72.019 536 61	4689633460047351296	11.35	12.10	12.84	11.28	5.17	0.03
6.516 75254	−71.889 833 56	4689650330681896320	10.34	11.22	12.18	10.28	22.14	0.05
5.189 98805	−72.077 528 65	4689806457019852160	10.82	11.62	12.43	10.76	9.63	0.06
6.253 87493	−72.343 920 27	4689573364861989760	11.10	11.89	12.68	11.04	6.88	0.04
5.311 94405	−72.250 633 22	4689612981641053696	10.76	11.57	12.41	10.70	9.61	0.06
5.223 78507	−72.226 704 00	4689613183491785856	11.45	12.21	12.95	11.39	4.38	0.02
5.971 92517	−71.786 636 49	4689837419442795648	10.8	11.61	12.44	10.74	8.72	0.05
5.875 16442	−72.376 748 22	4689572677667393664	9.74	10.86	12.39	9.71	47.97	–
6.618 72853	−71.836 899 44	4689651086596023040	11.26	12.02	12.78	11.19	5.13	0.03
5.680 86357	−71.775 175 46	4689848655076717440	11.53	12.27	12.99	11.47	5.53	0.05
7.066 00513	−72.150 843 34	4689582435832666752	10.07	11.05	12.18	10.00	43.35	–
6.613 44377	−71.795 584 20	4689652117388263296	10.88	11.68	12.49	10.82	7.67	0.08
6.739 45779	−71.820 542 82	4689651151009833728	10.84	11.65	12.48	10.77	11.22	0.15
5.413 39391	−72.414 063 04	4689595831823970304	10.18	11.10	12.13	10.12	97.15	–
6.621 13569	−71.666 164 31	4689844287094705408	13.91	14.51	15.03	13.84	3.76	0.01
6.795 59874	−72.519 100 46	4689558074778482304	10.44	11.30	12.24	10.38	14.25	0.05

Table 2, we listed the 34 eclipsing binaries. We cross-identified our list of eclipsing binaries with other catalogues in literature. We found six stars in common with the catalogue by Clement et al. (2001, updated to 2017), 13 listed also in the catalogue of eclipsing binaries based on OGLE data (Pawlak et al. 2016), and two in the GCVS catalogue (Samus' et al. 2017). The period distribution of the detected eclipsing binaries is peaked at ∼0.3–0.4 d, and ∼58 per cent of stars have $P<1$ d and are contact binaries.

Table 4. List of the analysed AGB stars in 47 Tuc.

α (J2000) (°)	δ (J2000) (°)	Gaia DR 2 ID	T	G	G_{BP}	G_{RP}	P (d)	σ_P (d)
		AGB						
6.016 888 95	−71.940 611 71	4689644798761947520	10.65	11.47	12.30	10.60	11.89	0.25
5.552 091 54	−72.095 830 82	4689641392838717568	12.10	12.73	13.29	12.04	30.93	0.08
6.476 970 44	−72.030 292 88	4689633975443492736	11.39	12.10	12.78	11.33	5.15	0.04
5.541 590 63	−72.055 439 71	4689642496660354048	11.45	12.18	12.88	11.39	4.74	0.07
5.968 552 92	−71.930 587 78	4689645039280106624	13.17	13.71	14.17	13.10	17.40	0.19
6.348 634 62	−72.202 152 39	4689622460621136256	11.83	12.50	13.11	11.77	3.14	0.03
5.840 931 94	−71.932 520 52	4689831264750937344	11.40	12.14	12.85	11.35	5.70	0.06
6.392 892 77	−71.959 792 83	4689641083606519168	11.64	12.32	12.96	11.58	3.78	0.04
5.470 650 91	−72.144 558 81	4689614867118928384	11.38	12.11	12.80	11.33	4.59	0.03
5.815 410 11	−71.898 967 96	4689832192474832000	11.11	11.86	12.59	11.06	4.00	0.04
6.345 886 23	−71.910 171 73	4689644592602980608	11.33	12.07	12.78	11.27	2.85	0.03
5.395 363 04	−72.140 503 45	4689617792004292096	12.06	12.71	13.29	12.00	1.87	0.02
5.505 750 90	−72.221 772 06	4689601746006553344	11.31	12.05	12.76	11.25	10.75	0.17
6.760 781 09	−72.021 210 70	4689633253888922624	13.10	13.67	14.15	13.04	4.88	0.02
6.598 801 35	−71.891 979 69	4689647405798359936	12.26	12.91	13.49	12.19	2.27	0.02
6.727 361 60	−72.227 443 07	4689580271169229824	12.27	12.93	13.52	12.22	1.87	0.01
5.554 213 78	−72.300 914 51	4689600332949678848	10.91	11.69	12.47	10.85	9.64	0.08
6.434 143 68	−72.314 881 55	4689573914617758336	12.15	12.80	13.40	12.09	1.89	0.01
6.952 943 26	−71.955 354 48	4689635178034205056	11.81	12.48	13.11	11.75	3.33	0.02
5.255 529 63	−72.316 046 82	4689600852653460352	11.59	12.28	12.92	11.54	4.64	0.02
7.137 141 70	−72.106 764 44	4689583294826108160	12.16	12.81	13.38	12.11	1.88	0.01
5.417 903 67	−72.387 291 62	4689596111009591936	12.27	12.91	13.47	12.21	1.72	0.01
5.304 465 52	−71.640 866 50	4689877654695832704	11.66	12.35	12.99	11.60	3.98	0.02
4.108 266 61	−72.355 876 40	4689607995176575488	11.53	12.24	12.92	11.47	4.66	0.08

4.2 RGB and AGB stars of 47 Tuc

We analysed the RGB stars members of 47 Tuc, that we flagged as candidate variable, to find their variability periods. To minimize the effects of the blends, we excluded from the analysis the RGB stars located at a distance <7.5 arcmin from the cluster centre. We also excluded all the stars that are blends, by comparing their light curves (and the periods found by GLS/AoV) with those of the neighbours located at a distance of 100 arcsec. After these selections, we saved 54 RGB stars with a good light curve. A sample of these light curves is shown in panels (a) of Fig. 13, while in panel (b) we show their position (red points) on the T versus $G_{BP} - G_{RP}$ CMD. We re-extracted the GLS periodograms for these light curves, but in this second iteration we looked for periods between 0.1 and 150 days. We listed the 54 RGB stars, their astrophotometric properties and their periods in Table 3.

In this paper, we extend the work by Lebzelter et al. (2005): they analysed the long period, pulsating stars located on the tip of the RGB in the period–luminosity (PL) plan. Because of the uncertainties on their photometric series, their study was limited to stars with $V \lesssim 12$. Thanks to the high quality of our light curves, we are able to extend the PL distribution to fainter magnitudes ($T \sim 15.1$). Panel (c) of Fig. 13 shows the relation between T magnitude and the period for the RGB stars analysed by Lebzelter et al. (2005, azure squares) and by us (red points):[5] the two distributions are superimposed. In the range $9.5 \lesssim T \lesssim 12.0$, the period is proportional to the luminosity of the stars. In the range $12.0 \lesssim T \lesssim 15.5$ we found the unexpected result that the period is inversely proportional to the luminosity. For completeness, we show the relation period–colour (PC) in panel (d) of Fig. 13: for $(G_{BP} - G_{RP}) \gtrsim 1.5$ the period grows with the colour, while for $(G_{BP} - G_{RP}) \lesssim 1.5$ the period decreases with the colour.

We did the same analysis with the asymptotic giant-branch (AGB) stars members of 47 Tuc. We found 24 AGB variable stars with good light curves; they are listed in Table 4. We derived the period by using the GLS periodogram and looking for periods between 0.1 and 150 d. Finally, we analysed the PL and PC distributions. Fig. 14 summarizes the results. Panels (c) and (d) show that the PL and PC distributions for AGB (in green) and RGB (in red) stars are superimposed.

A detailed analysis of the PL/PC distributions for AGB and RGB stars in globular clusters is beyond the scope of this work and might be the subject of a future analysis based on our released light curves.

5 COMPARISON WITH OTHER PIPELINES

At present, the most advanced pipeline aimed at the extraction of any kind of light curve from FFIs is `eleanor` (Feinstein et al. 2019). In this section, we compare the quality of our photometry with that obtained by `eleanor`, highlighting the importance of neighbour subtraction when we consider crowded environments. Fig. 15 shows six different raw light curves of stars with different luminosities and located in environments characterized by different levels of crowding. Panels on the right show that the contamination by neighbour stars in the cases (a) (Gaia DR2 4689720939927488768, $T \sim 7.7$), (d) (Gaia DR2 4689760969022718720, $T \sim 13.1$), and (e) (Gaia DR2 4689953108681026304, $T \sim 15.6$) is low, and the raw light curves output of the PATHOS pipeline (left panels, in blue) and `eleanor` pipeline (middle panels, in red) are similar. The light curves were extracted by using the same photometric

[5]Only one star is in common to both the samples, and the period found by Lebzelter et al. (2005) and by us differs of ∼1 d.

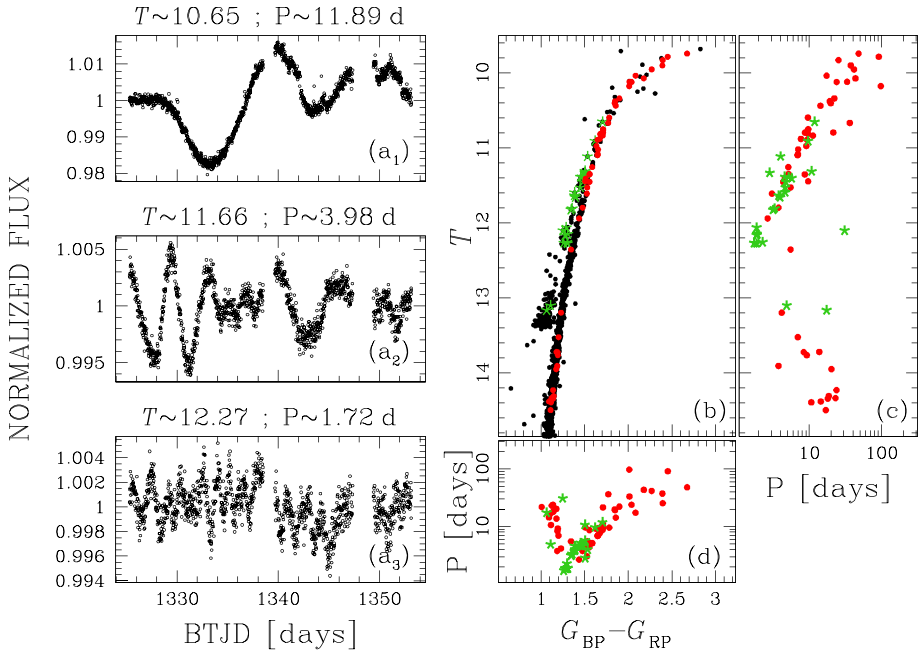

Figure 14. Analysis of AGB stars. Panels (a_1)–(a_3) show a sample of light curves of AGB stars, ordered by magnitude. Panel (b) shows T versus $G_{BP} - G_{RP}$ CMD; panel (c) and (d) the PL and the PC relations. In panels (b), (c), and (d) red circles and green starred points are RGB and AGB stars, respectively.

apertures. In crowded environments, the dilution and contamination by neighbour stars affect the quality of the light curves extracted with `eleanor`. In the case (b) (Gaia DR2 4701817938655245568, $T \sim 10.5$), the bright neighbour star dilutes the light of the target star during the eclipses, with the result that the observed depth of the eclipses is lower. This effect is important especially in the light curve analysis of candidate transiting exoplanets: without considering the dilution effects due to neighbour stars, the radius of the candidate exoplanet would be underestimated. In the cases (c) (Gaia DR2 4689837419442795648, $T \sim 10.8$) and (f) (Gaia DR2 4689619853580301824, $T \sim 15.9$) the presence of many neighbour stars strongly affects the shape and the quality of the light curve of the target star; in particular, in the case (f) the variability of the target star is significantly diluted by the light of the neighbour stars.

6 THE DATA RELEASE

We publicly release all the light curves extracted in this work. The light curves will be available in the Mikulski Archive for Space Telescopes (MAST) as a High Level Science Product (HLSP) via https://doi.org/10.17909/t9-es7m-vw14. Each light curve contains the epoch in BTJD, the five extracted photometries (PSF-fitting, 1-pixel, 2-pixel, 3-pixel, 4-pixel aperture), the value of the local sky, the position (x, y) on the image, and the data quality flag (see section 9 of the TESS Science Data Products Description Document,[6] for details). Light curves are both in `ascii` and `fits` format, which header contains information on the star (from the Gaia DR2 catalogue) and on its observations.

[6]https://archive.stsci.edu/missions/tess/doc/EXP-TESS-ARC-ICD-TM-0014.pdf

7 SUMMARY

In this work, we presented our PSF-based approach, applied for the first time to *TESS* FFIs, in order to extract light curves of stars in a crowded field centred on 47 Tuc. The pipeline presented in this pilot work is essential for the success of the PATHOS project, whose main scope is the analysis of high-precision light curves of stellar cluster members, in order to find candidate exoplanets orbiting bright cluster stars and variable stars.

Discovering and characterizing exoplanets in stellar clusters (especially open clusters and young associations) represent an important ingredient to understand how exoplanet systems have formed and evolved. At variance with what happens for most Galactic field stars, cluster star parameters (such as age, mass, and chemical composition) are generally well determined with high accuracy. This allows us to correlate stellar parameters (such as stellar mass) with exoplanet characteristics. Furthermore, hundreds of stellar clusters populate the Milky Way (Cantat-Gaudin et al. 2016), having ages that span from few tens Myrs to ∼10 Gyrs (Bossini et al. 2019) and showing a wide variety of chemical compositions. Combining pieces of information on stellar clusters with exoplanet properties (and with the rate of exoplanets in stellar clusters), it will be possible to understand how ages of stars, and the environment in which they are embedded, have affected the formation and evolution of exoplanets.

In this pilot project we have extracted, corrected, and analysed the light curves of 16641 stars in a field containing the globular cluster 47 Tuc. These stars belong either to 47 Tuc, or the Milky Way, or the SMC. We took advantage of the Gaia DR2 catalogue to extract not only astrophotometric data of stars located in this region, but also, when possible, stellar parameters. We searched for transit signals among the extracted light curves and we found and characterized a candidate transiting exoplanet orbiting a MS field star. This candidate exoplanet, named PATHOS-1, is not in the list of *TESS* Objects

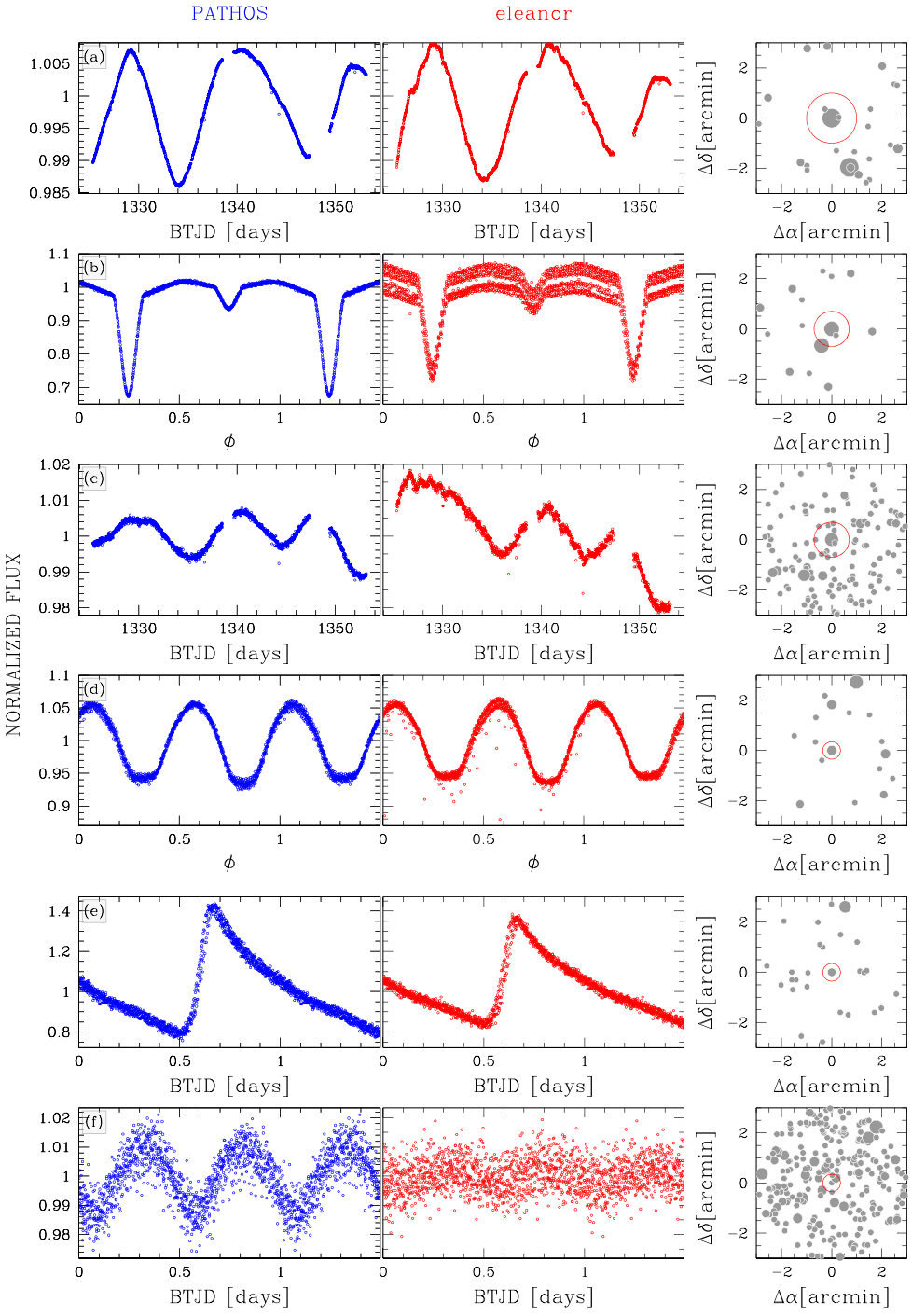

Figure 15. Comparison between the raw light curves extracted with the PATHOS pipeline (in blue, left-hand panels) and the `eleanor` pipeline (in red, middle panels). Right-hand panels show the finding charts of the target stars, obtained by using the Gaia DR2 data: in red the size of the aperture used for the extraction of the light curves. The light curves are sorted by magnitude.

of Interest (TOI)[7] and is a new discovery. No candidate transiting exoplanets have been found around bright RGB stars of 47 Tuc; given the nature of RGB stars, the probability of finding exoplanets orbiting them and having periods <27 days, is low. We also searched for variables among the stars in the analysed field. We analysed the 34 eclipsing binaries in the field and the relations PL and PC for the RGB and AGB stars members of 47 Tuc. We found that the period of variability for AGB and RGB stars is proportional to the luminosity above the mean magnitude of the RGB bump, but we found also that below the RGB bump the period decreases as the stellar brightness increases.

The raw and corrected light curves will be uploaded on the MAST archive as HLSP. In this way, they will always be available to the astronomical community for any scientific goal.

[7] https://tev.mit.edu/toi/

ACKNOWLEDGEMENTS

PATHOS data products are available at MAST: http://archive.stsci.edu/hlsp/pathos.

DN and GP acknowledge partial support by the Università degli Studi di Padova Progetto di Ateneo BIRD178590. LB received support from Italian Space Agency (ASI) regulated by 'Accordo ASI-INAF n. 2013-016-R.0 del 9 Luglio 2013 e integrazione del 9 Luglio 2015'. VG, MM, and GP recognize partial support from the Italian Space Agency (ASI), regulated by 'Accordo ASI-INAF n. 2015-019-R.0 del 29 Luglio 2015". LRB acknowledges support by MIUR under PRIN program #2017Z2HSMF. GL acknowledges support by CARIPARO Foundation, according to the agreement CARIPARO-Università degli Studi Di Padova, Pratica n. 2018/0098. Stacked image is obtained by using `SWarp` (Bertin et al. 2002) and `ASTROMETRY.NET` codes (Lang et al. 2010). Some tasks of the data reduction and analysis have been carried out using `PARALLEL` (Tange 2011) and `VARTOOLS` v. 1.36 (Hartman & Bakos 2016).

REFERENCES

Aigrain S., Parviainen H., Pope B. J. S., 2016, MNRAS, 459, 2408
Anderson J., Bedin L. R., Piotto G., Yadav R. S., Bellini A., 2006, A&A, 454, 1029
Armstrong D. J. et al., 2016, MNRAS, 456, 2260
Baglin A. et al., 2006, 36th COSPAR Scientific Assembly. Beijing, China, p. 3749
Barros S. C. C., Demangeon O., Deleuil M., 2016, A&A, 594, A100
Benatti S. et al., 2019, A&A, 630, A81
Bertin E., Mellier Y., Radovich M., Missonnier G., Didelon P., Morin B., 2002, in Bohlender D. A., Durand D., Handley T. H., eds, ASP Conf. Ser. Vol. 281, Astronomical Data Analysis Software and Systems XI, Astron. Soc. Pac., San Francisco, p. 228
Borsato L. et al., 2019, MNRAS, 484, 3233
Borucki W. J. et al., 2010, Science, 327, 977
Bossini D. et al., 2019, A&A, 623, A108
Brucalassi A. et al., 2014, A&A, 561, L9
Brucalassi A. et al., 2017, A&A, 603, A85
Cantat-Gaudin T., Donati P., Vallenari A., Sordo R., Bragaglia A., Magrini L., 2016, A&A, 588, A120
Claret A., 2018, A&A, 618, A20
Clement C. M. et al., 2001, AJ, 122, 2587
Feinstein A. D. et al., 2019, PASP, 131, 094502
Foreman-Mackey D., Hogg D. W., Lang D., Goodman J., 2013, PASP, 125, 306
Gaia Collaboration et al., 2018, A&A, 616, A1
Gilliland R. L. et al., 2011, ApJS, 197, 6
Gilliland R. L., Chaplin W. J., Jenkins J. M., Ramsey L. W., Smith J. C., 2015, AJ, 150, 133
Goldsbury R., Richer H. B., Anderson J., Dotter A., Sarajedini A., Woodley K., 2010, AJ, 140, 1830
Greisen E. W., Calabretta M. R., 2002, A&A, 395, 1061
Hartman J. D., Bakos G. Á., 2016, Astron. Comput., 17, 1
Hippke M., Heller R., 2019, A&A, 623, A39
Howell S. B. et al., 2014, PASP, 126, 398
Kipping D. M., 2013, MNRAS, 435, 2152
Kovács G., Zucker S., Mazeh T., 2002, A&A, 391, 369
Kreidberg L., 2015, PASP, 127, 1161
Lang D., Hogg D. W., Mierle K., Blanton M., Roweis S., 2010, AJ, 139, 1782
Lebzelter T., Wood P. R., Hinkle K. H., Joyce R. R., Fekel F. C., 2005, A&A, 432, 207
Libralato M., Bedin L. R., Nardiello D., Piotto G., 2016a, MNRAS, 456, 1137
Libralato M. et al., 2016b, MNRAS, 463, 1780
Malavolta L. et al., 2016, A&A, 588, A118
Mann A. W. et al., 2018, AJ, 155, 4
Moré J. J., Garbow B. S., Hillstrom K. E., 1980, Technical Report ANL-80-74, User guide for MINPACK-1. Argonne Nat. Lab, Argonne, IL
Nardiello D. et al., 2015, MNRAS, 447, 3536
Nardiello D., Libralato M., Bedin L. R., Piotto G., Ochner P., Cunial A., Borsato L., Granata V., 2016a, MNRAS, 455, 2337
Nardiello D., Libralato M., Bedin L. R., Piotto G., Borsato L., Granata V., Malavolta L., Nascimbeni V., 2016b, MNRAS, 463, 1831
Pál A., Molnár L., Kiss C., 2018, PASP, 130, 114503
Pawlak M. et al., 2016, AcA, 66, 421
Pollacco D. L. et al., 2006, PASP, 118, 1407
Quinn S. N. et al., 2012, ApJ, 756, L33
Quinn S. N. et al., 2014, ApJ, 787, 27
Ricker G. R. et al., 2015, J. Astron. Telescopes Instrum. Syst., 1, 014003
Riess A. G. et al., 2018, ApJ, 861, 126
Samus' N. N., Kazarovets E. V., Durlevich O. V., Kireeva N. N., Pastukhova E. N., 2017, Astron. Rep., 61, 80
Schwarzenberg-Czerny A., 1989, MNRAS, 241, 153
Shupe D. L., Moshir M., Li J., Makovoz D., Narron R., Hook R. N., 2005, in Shopbell P., Britton M., Ebert R., eds, ASP Conf. Ser. Vol. 347, Astronomical Data Analysis Software and Systems XIV. Astron. Soc. Pac., San Francisco, p. 491
Soares-Furtado M., Hartman J. D., Bakos G. Á., Huang C. X., Penev K., Bhatti W., 2017, PASP, 129, 044501
Tange O., 2011, login: The USENIX Magazine, 36, 42
Twicken J. D. et al., 2018, PASP, 130, 064502
Udalski A., Szymanski M., Kaluzny J., Kubiak M., Mateo M., 1992, AcA, 42, 253
Vallely P. J. et al., 2019, MNRAS, 487, 2372
Van Cleve J. E. et al., 2016, PASP, 128, 075002
Vanderburg A., Johnson J. A., 2014, PASP, 126, 948
Zechmeister M., Kürster M., 2009, A&A, 496, 577

SUPPORTING INFORMATION

Supplementary data are available at *MNRAS* online.

http://archive.stsci.edu/hlsp/pathos

Please note: Oxford University Press is not responsible for the content or functionality of any supporting materials supplied by the authors. Any queries (other than missing material) should be directed to the corresponding author for the article.

This paper has been typeset from a TEX/LATEX file prepared by the author.